ISSN 1674-1056
http://cpb.iphy.ac.cn
http://iopscience.iop.org/cpb
中国物理 B
Chinese Physics
中国物理
Chinese Physics B

Quantitative rescattering theory for nonsequential double ionization

Zhangjin Chen(陈长进), Fang Liu(刘芳), Hua Wen(文华)
Citation: Chin. Phys. B . 2019, 28(12): 123401 . **doi:** 10.1088/1674-1056/ab54b3
Journal homepage: http://cpb.iphy.ac.cn; http://iopscience.iop.org/cpb

What follows is a list of articles you may be interested in

X-ray emission from 424-MeV/u C ions impacting on selected target

Xian-Ming Zhou(周贤明), Rui Cheng(程锐), Yu Lei(雷瑜), Yuan-Bo Sun(孙渊博), Yu-Yu Wang(王瑜玉), Xing Wang(王兴), Ge Xu(徐戈), Ce-Xiang Mei(梅策香), Xiao-An Zhang(张小安), Xi-Meng Chen(陈熙萌), Guo-Qing Xiao(肖国青), Yong-Tao Zhao(赵永涛)
Chin. Phys. B . 2016, 25(2): 023402 . **doi:** 10.1088/1674-1056/25/2/023402

Triple differential cross sections of magnesium in doubly symmetric geometry

S Y Sun(孙世艳), X Y Miao(苗向阳), Xiang-Fu Jia(贾祥富)
Chin. Phys. B . 2016, 25(1): 013401 . **doi:** 10.1088/1674-1056/25/1/013401

Fast-electron-impact study on excitations of 4d electron of xenon

Zhang Xin, Liu Ya-Wei, Peng Yi-Geng, Xu Long-Quan, Ni Dong-Dong, Kang Xu, Wang Yang-Yang, Qi Yue-Ying, Zhu Lin-Fan
Chin. Phys. B . 2015, 24(12): 123401 . **doi:** 10.1088/1674-1056/24/12/123401

Theoretical simulation of the photoassociation process for NaCs

Zhang Chang-Zhe, Zheng Bin, Wang Jun, Meng Qing-Tian
Chin. Phys. B . 2013, 22(2): 023401 . **doi:** 10.1088/1674-1056/22/2/023401

High sensitive detection of high-order partial wave scattering in photoassociation of ultralcold atoms

Li Yu-Qing,Ma Jie,Wu Ji-Zhou,Zhang Yi-Chi,Zhao Yan-Ting,Wang Li-Rong,Xiao Lian-Tuan,Jia Suo-Tang
Chin. Phys. B . 2012, 21(4): 043404 . **doi:** 10.1088/1674-1056/21/4/043404

TOPICAL REVIEW — Strong-field atomic and molecular physics

Quantitative rescattering theory for nonsequential double ionization*

Zhangjin Chen(陈长进)†, Fang Liu(刘芳), and Hua Wen(文华)

Department of Physics, College of Science, Shantou University, Shantou 515063, *China*

(Received 7 July 2019; revised manuscript received 23 October 2019; published online 29 November 2019)

We review the recently improved quantitative rescattering theory for nonsequential double ionization, in which the lowering of threshold due to the presence of electric field at the time of recollision has been taken into account. First, we present the basic theoretical tools which are used in the numerical simulations, especially the quantum theories for elastic scattering of electron as well as the processes of electron impact excitation and electron impact ionization. Then, after a brief discussion about the properties of the returning electron wave packet, we provide the numerical procedures for the simulations of the total double ionization yield, the double-to-single ionization ratio, and the correlated two-electron momentum distribution.

Keywords: laser-induced recollision, nonsequential double ionization, quantitative rescattering model

PACS: 34.50.Rk, 34.80.Dp, 32.80.Fb, 32.80.Rm **DOI:** 10.1088/1674-1056/ab54b3

1. Introduction

Nonsequential double ionization (NSDI) of atoms in strong laser fields has attracted considerable interest both experimentally and theoretically for more than three decades, and still remains one of the most interesting and challenging topics in strong-field physics. The interest on NSDI was first stimulated by the early measurements of the number of doubly charged ions of rare gas atoms exposed to intense laser pulses versus the peak laser intensity.[1–5] The characteristic "knee" structure observed in experiment provides the distinct evidence for NSDI since double-ionization yields could be several orders of magnitude greater than the prediction by the standard theory based on the assumption that electrons are emitted one by one, with the second ionization independent of the previous one. However, with the only available experimental data for the total yield of doubly charged ion, the mechanisms responsible for the two-electron transition were still a matter of controversy. For example, it was suggested that the second electron could be shaken-off by a nonadiabatic change of the potential caused by the emission of the first electron.[3] Alternatively, it was argued[6] that the first electron, released by tunneling through the potential barrier of the combined atomic and field potential, is driven back to its parent ion by the laser field and ionizes the second electron, in a process analogous to an $(e,2e)$ collision. The debate on the mechanisms responsible for NSDI was further settled by the differential ionization measurements, which were first carried out at the turn of this century, for momentum distributions of the doubly charged ion along the laser polarization direction[7] and the momentum correlations between the two outgoing electrons.[8] Those differential ionization measurements provide more detailed insight into the dynamics of the NSDI process and provide a much improved testing ground for the different theoretical models in the dispute. Nowadays, it has already been widely accepted that the main mechanisms leading to NSDI are the laser-induced recollisional $(e,2e)$ and the recollisional excitation with subsequent ionization of the second electron from the excited state of the parent ion.[9]

Over the past three decades, there have been no shortage of theoretical efforts devoted to NSDI (for a review, see Refs. [10] and [11]). It has been well recognized that five interactions are involved in NSDI: the interactions of the laser field with the two electrons, the Coulomb interactions between the doubly charged ion and the two outgoing electrons, and the electron–electron interaction. All the five interactions are strong and roughly equal in importance, so ideally they must be treated on an equal basis. However, in actual numerical calculations, one has to resort to simplifying approximations to make the calculations tractable. In general, the numerical methods developed for NSDI fall into two categories. The first approach takes the set of fundamental interactions of the electrons and solves the time dependent Schrödinger equation (TDSE) or the time dependent Newton equations (TDNE) for the motion of the two electrons. Indeed, a complete description of NSDI could be obtained by an exact solution of the TDSE. However, it is still a formidable computational challenge because of computer speed and memory requirements, and the results alone would not offer much insight into the basic mechanisms for the double ionization processes. So far, only a very few TDSE calculations, with more or less ap-

*Project supported by the National Natural Science Foundation of China (Grant No. 11274219), the Science and Technology Planning Project of Guangdong Province of China (Grant No. 180917124960522), and the Program for Promotion of Science at Universities in Guangdong Province of China (Grant No. 2018KTSCX062).

†Corresponding author. E-mail: chenzj@stu.edu.cn

© 2019 Chinese Physical Society and IOP Publishing Ltd

proximations, have been carried out for NSDI.[12–15] On the contrary, it is easier to solve the TDNE for NSDI,[16] and a number of predictions with at least semiquantitative agreement with a relatively wide variety of experimental data have been achieved.[17,18] The second approach is based on the rescattering model from which conceptual clarity derives more easily, even though this might come at the expense of possible loss of physical reality. Within this framework, the *S*-matrix theory was first developed by extending the strong field approximation (SFA) for high order above threshold ionization (HATI)[19,20] to double ionization.[21] While the TDSE results contain all possible outcomes, which are mixed together, from a given initial state, the *S*-matrix theory allows one to select any particular item, and hence is more powerful in identifying the specific mechanisms of the NSDI process. Similarly, a recently developed full quantum theory for NSDI, called quantitative rescattering (QRS) model, is also based on the rescattering model. While laser-induced rescattering processes can be qualitatively interpreted by the classical rescattering model,[6,22] the QRS model provides the quantitative description. In addition, the semiclassical theory including the tunneling effect, indeed, has also been widely recognized as a useful approach to simulate the NSDI.[23–27]

The QRS model was first proposed for HATI,[28,29] in which the momentum distribution of the HATI photoelectron is factorized as a product of the returning electron wave packet (RWP) and the differential cross sections (DCS) for elastic scattering of the returning electron with the parent ion. The only difference between HATI and NSDI is that the returning electron experiences different types of collisions, one is elastic scattering and the other is inelastic scattering including electron impact ionization and electron impact excitation. Based on this philosophy, the QRS model was extended to NSDI.[30–32] The past decade has witnessed great success of the QRS model in dealing with various laser-induced rescattering processes.[33,34] Recently, the QRS model for NSDI has been further improved[35–39] by taking into account the lowering of threshold due to the presence of electric field at the instant of recollision.[40]

In this review, we will limit ourselves to the presentation of the improved QRS model for NSDI and its applications to some of the major experimental observations. This article is organized as follows. In Section 2, we will review the basic theoretical tools used in the numerical simulations. In Section 3, we will present the numerical procedures for the simulations of the total yield of doubly charged ion, the double-to-single ionization ratio, and the correlated two-electron momentum distribution. Finally, a summary and outlook will be given in Section 4.

Unless indicated otherwise, atomic units (a.u.) are used throughout this paper.

2. Basic theoretical tools

2.1. Theoretical model for single ionization rate

Ionization of atoms is the first step of the laser-induced rescattering processes such as HATI,[41] high-order harmonic generation (HHG),[42] and NSDI.[5,8]

In general, two mechanisms have been classified for ionization of atoms exposed to an intense laser field by using the Keldysh parameter[43] $\gamma = \sqrt{I_{\rm p}/(2U_{\rm p})}$, where $I_{\rm p}$ is the ionization potential and $U_{\rm p}$ is the ponderomotive energy. In the multiphoton ionization regime when $\gamma > 1$, an atom absorbs more photons than the minimum number required for the ejection of an electron, leading to the the characteristic above-threshold ionization (ATI) peaks in the photoelectron energy spectra which are separated by the photon energy, while their positions are shifted by the ponderomotive potential. On the other hand, at higher laser intensities, when $\gamma < 1$, the liberation of an electron is understood to proceed through tunneling ionization.

The most commonly used theory for ionization of atoms by a linearly polarized laser field is the Ammosov–Delone–Kainov (ADK) approach,[44] which is generally valid for tunneling ionization when the adiabaticity parameter γ is lower than 1.

Suppose an atom is exposed to a linearly polarized laser pulse (along the z axis) with carrier frequency ω and the carrier envelope phase (CEP) φ, the field can be expressed as

$$\boldsymbol{F}(t) = \hat{z}F_0 \cos^2\left(\frac{\pi t}{\tau}\right)\cos(\omega t + \varphi) \tag{1}$$

for the time interval $(-\tau/2, \tau/2)$ and zero elsewhere. According the ADK model, the ionization rate of the atom at time t is given by

$$W_{\rm ADK}[|F(t)|] = |C_{n^*l^*}|^2 f(l,m) I_{\rm p}\left[\frac{2\kappa}{|F(t)|}\right]^{2n^*-|m|-1} \times \exp\left[\frac{-2\kappa}{3|F(t)|}\right], \tag{2}$$

where

$$|C_{n^*l^*}|^2 = \frac{2^{2n^*}}{n^*\Gamma(n^*+l^*+1)\Gamma(n^*-l^*)}, \tag{3}$$

$$f(l,m) = \frac{(2l+1)(l+|m|)!}{2^{|m|}|m|!(l-|m|)!}. \tag{4}$$

In the above equations, $\kappa = (2I_{\rm p})^{3/2}$, $n^* = Z_{\rm c}(2I_{\rm p})^{-1/2}$ is the effective quantum number with $Z_{\rm c}$ being the charge of the residual ion, $l^* = n^* - 1$ is the effective orbital quantum number, and l and m are the orbital and magnetic quantum numbers of the valence electron of the atom, respectively.

The ADK model has also been generalized to molecular systems.[45] However, Tong and Lin[46] found that the ADK rates significantly overestimate the numerically calculated static ionization rates for atoms in the barrier-suppression

regime, hence they modified the original ADK model to extend the ADK rates from the tunneling ionization region to the near- and over-the-barrier regimes by introducing an empirical correction factor. The modified ADK rate $w[|F(t)|]$ is given by[46]

$$W_{\mathrm{MADK}}[|F(t)|] = W_{\mathrm{ADK}}[|F(t)|]\,\mathrm{e}^{-\mu(Z_c^2/I_\mathrm{p})(|F(t)|/\kappa)}. \quad (5)$$

The fitted parameter μ in Eq. (5) for a few atoms and ions has been given in Ref. [46], which is in the range of $6 < \mu < 10$.

The ADK model represents the limit when $\gamma \to 0$ of the theory proposed by Perelomov, Popov, and Terent'ev (PPT),[47] which is valid for arbitrary γ values. In the PPT model, the ionization rate reads

$$\begin{aligned} & W_{\mathrm{PPT}}[|F(t)|,\omega] \\ = \; & |C_{n^*l^*}|^2 f(l,m) I_\mathrm{p} \left[\frac{2\kappa}{|F(t)|}\right]^{2n^*-|m|-1} (1+\gamma^2)^{|m|/2+3/4} \\ & \times A_m(\omega,\gamma)\exp\left[\frac{-2\kappa}{3|F(t)|}g(\gamma)\right], \end{aligned} \quad (6)$$

where

$$g(\gamma) = \frac{3}{2\gamma}\left[\left(1+\frac{1}{2\gamma^2}\right)\sinh^{-1}\gamma - \frac{\sqrt{1+\gamma^2}}{2\gamma}\right]. \quad (7)$$

The details about the coefficients $A_m(\omega,\gamma)$ in Eq. (6) can be found in Refs. [48] and [49].

With the calculated ionization rate, one can obtain the total ionization probability by a laser pulse as

$$P_m = 1 - \mathrm{e}^{-\int_{-\infty}^{+\infty} W_m[|F(t)|]\mathrm{d}t}, \quad (8)$$

where m stands for ADK, MADK, or PPT.

2.2. The strong field approximation

The strong field approximation is a very effective tool to deal with the interaction of atoms with strong laser field. While the SFA can also be used to obtained the total ionization probability of an atom by a laser pulse, it further provides a fairly good quantitative description of the photoenergy spectra as well as the momentum distributions. In general, the SFA model is valid when $I_\mathrm{p} \le 2U_\mathrm{p}$. This condition implies that when the electron appears in the continuum it is only under the influence of a very strong laser field. In addition, when the electron comes back to the parent ion it has a large kinetic energy, so that the Coulomb force of the atomic potential can be neglected.

In the length gauge and the dipole approximation, the laser–electron interaction can be expressed by

$$H_\mathrm{i}(t) = \boldsymbol{r}\cdot\boldsymbol{F}(t). \quad (9)$$

Within this approximation, the exact expression for the probability amplitude of detecting an ATI electron with momentum $\boldsymbol{p}$ and kinetic energy $E = p^2/2$ can be written formally as[50]

$$f(\boldsymbol{p}) = -\mathrm{i}\lim_{t\to\infty}\int_{-t}^{t}\mathrm{d}t'\left\langle\Psi_{\boldsymbol{p}}(t)\left|U(t,t')H_\mathrm{i}(t')\right|\Psi_0(t')\right\rangle, \quad (10)$$

where $\Psi_0(t)$ and $\Psi_{\boldsymbol{p}}(t)$ are the ground state and a scattering state with asymptotic $\boldsymbol{p}$, respectively, of the atomic Hamiltonian

$$H_\mathrm{a} = -\frac{1}{2}\nabla^2 + V(\boldsymbol{r}), \quad (11)$$

and $U(t,t')$ is the time-evolution operator of the complete Hamiltonian

$$H(t) = H_\mathrm{a} + H_\mathrm{i}(t). \quad (12)$$

The time-evolution operator satisfies the Dyson equation

$$U(t,t') = U_\mathrm{F}(t,t') - \mathrm{i}\int_{t'}^{t}\mathrm{d}t'' U_\mathrm{F}(t,t'')VU(t'',t'), \quad (13)$$

where $U_\mathrm{F}(t,t')$ is the time-evolution operator corresponding to the Hamiltonian of a free electron in the laser field, which is

$$H_\mathrm{F} = -\frac{1}{2}\nabla^2 + H_\mathrm{i}(t). \quad (14)$$

The eigenstates of the time-dependent Schrödinger equation with the Hamiltonian $H_\mathrm{F}(t)$ are the Volkov states

$$|\chi_{\boldsymbol{p}}(t)\rangle = |\boldsymbol{p}+\boldsymbol{A}(t)\rangle\exp[-\mathrm{i}S_{\boldsymbol{p}}(t)], \quad (15)$$

where $\boldsymbol{A}(t)$ is the vector potential of the laser field $\boldsymbol{F}(t)$, $|\boldsymbol{k}\rangle$ denotes a plane wave state

$$\langle\boldsymbol{r}|\boldsymbol{k}\rangle = \frac{1}{(2\pi)^{3/2}}\exp(\mathrm{i}\boldsymbol{k}\cdot\boldsymbol{r}), \quad (16)$$

and the action $S_{\boldsymbol{p}}(t)$ reads

$$S_{\boldsymbol{p}}(t) = \frac{1}{2}\int_{-\infty}^{t}\mathrm{d}t'\left[\boldsymbol{p}+\boldsymbol{A}'(t)\right]^2. \quad (17)$$

The Volkov time-evolution operator is then given by

$$U_\mathrm{F}(t,t') = \int\mathrm{d}\boldsymbol{k}\,|\chi_{\boldsymbol{k}}(t)\rangle\left\langle\chi_{\boldsymbol{k}}(t')\right|. \quad (18)$$

Introducing the strong field approximation, i.e., replacing $\langle\Psi_{\boldsymbol{p}}(t)|U(t,t')$ with $\langle\chi_{\boldsymbol{k}}(t)|U(t,t')$ in Eq. (10), and truncating the full time-evolution operator $U(t,t')$ after the second term, one obtains the SFA ionization amplitude as

$$f_{\mathrm{SFA}}(\boldsymbol{p}) = f^{(1)}_{\mathrm{SFA}}(\boldsymbol{p}) + f^{(2)}_{\mathrm{SFA}}(\boldsymbol{p}), \quad (19)$$

where the first term

$$f^{(1)}_{\mathrm{SFA}}(\boldsymbol{p}) = -\mathrm{i}\int_{-\infty}^{\infty}\mathrm{d}t\,\langle\chi_{\boldsymbol{p}}(t)\,|H_\mathrm{i}(t)|\,\Psi_0(t)\rangle \quad (20)$$

corresponds to the standard SFA, and the second term

$$\begin{aligned} f^{(2)}_{\mathrm{SFA}}(\boldsymbol{p}) \; = \; & -\int_{-\infty}^{\infty}\mathrm{d}t\int_{t}^{\infty}\mathrm{d}t'\int\mathrm{d}\boldsymbol{k}\,\langle\chi_{\boldsymbol{p}}(t')\,|V|\,\chi_{\boldsymbol{k}}(t')\rangle \\ & \times\langle\chi_{\boldsymbol{k}}(t)\,|H_\mathrm{i}(t)|\,\Psi_0(t)\rangle \end{aligned} \quad (21)$$

is the first order correction to the standard SFA which consists of ionization, propagation in the continuum, and the interaction of the returning electron with the parent ion.

The form of $f_{\rm SFA}(\boldsymbol{p})$ in Eq. (19) allows one to identify the contribution from each individual term. If $f^{(2)}_{\rm SFA}(\boldsymbol{p})$ is dropped in Eq. (19), the standard SFA result can be obtained. For convenience, the standard SFA is referred to as SFA1, while the result from keeping $f^{(2)}_{\rm SFA}(\boldsymbol{p})$ only in Eq. (19) is referred to as SFA2.[20] The details of numerical procedures for evaluation of the probability amplitude have been presented in Refs. [19], [20], and [51].

It should be noted that, in the numerical calculations, one needs to use a short-range potential

$$\tilde{V}(\boldsymbol{r}) = V(\boldsymbol{r})\,{\rm e}^{-\alpha r}, \tag{22}$$

where α is a parameter introduced to avoid the singularity in $f^{(2)}_{\rm SFA}(\boldsymbol{p})$.

The angular and momentum distribution of an electron emitted in the direction of $\hat{\boldsymbol{p}}$ is given by

$$\frac{{\rm d}^3P_{\rm SFA}}{{\rm d}p_x{\rm d}p_y{\rm d}p_z} = |f_{\rm SFA}(\boldsymbol{p})|^2. \tag{23}$$

For a linearly polarized laser field, the system has cylindrical symmetry. As a result, the two-dimensional momentum distribution is defined as

$$\frac{{\rm d}^2P_{\rm SFA}}{{\rm d}p_\perp{\rm d}p_z} = |f_{\rm SFA}(\boldsymbol{p})|^2 2\pi p\sin\theta, \tag{24}$$

where $p_\perp = \sqrt{p_x^2+p_y^2}$ and θ is the angle between the polarization axis of the laser field and the direction of the ejected photoelectron. Obviously, the integration over the azimuthal angle φ has been carried out in Eq. (24). Furthermore, by integrating over θ, we obtain the energy spectra

$$\frac{{\rm d}P_{\rm SFA}}{{\rm d}E} = 2\pi\sqrt{2E}\int_{-1}^{+1}|f_{\rm SFA}(\boldsymbol{p})|^2{\rm d}(\cos\theta). \tag{25}$$

It should be noted that the numerical results depend on the screening factor α. It has been found that the photoelectron energy spectra of SFA2 at low energies increase very rapidly as α decreases. Nevertheless, in the high energy regime, when $E > 4U_{\rm p}$, the dependence becomes relatively weak, and the shape of the energy spectra almost remains the same. Usually, in the numerical calculations, the value of α is chosen in such a way that direct ionization (SFA1) dominates the photoelectron spectra for the energies bellow $2U_{\rm p}$.[52,53]

2.3. The time-dependent Schrödinger equation

While the SFA allows for intuitive physical interpretation of the intense laser–atom interaction, the numerical solutions of the time-dependent Schrödinger equation, in principle, provide a full quantum description of various phenomena, including the ATI spectra, for an atom in a strong laser field. Within the single-active-electron approximation, the TDSE for single ionization of an atom in the presence of a linearly polarized laser field can be written, in the length gauge, as

$${\rm i}\frac{\partial}{\partial t}\Psi(\boldsymbol{r},t) = [H_{\rm a}+H_{\rm i}(t)]\Psi(\boldsymbol{r},t), \tag{26}$$

where $H_{\rm i}$ and $H_{\rm a}$ are the laser–electron interaction and the atomic Hamiltonian given by Eqs. (9) and (11), respectively. The above time-dependent equation is solved by using a second-order split operator method[54,55]

$$\Psi(\boldsymbol{r},t+\Delta t) = {\rm e}^{-{\rm i}H_{\rm a}\Delta t/2}\,{\rm e}^{-{\rm i}H_{\rm i}(t+\Delta t/2)\Delta t}\,{\rm e}^{-{\rm i}H_{\rm a}\Delta t/2}\Psi(\boldsymbol{r},t), \tag{27}$$

and the wave function is expanded by the direct products of discrete variable representation basis sets[56–58] associated with the Legendre polynomials.

The probability amplitude is obtained by projecting the total final wave function at the end of the laser pulse onto eigenstates of a continuum electron with momentum $\boldsymbol{p}$

$$f_{\rm TDSE}(\boldsymbol{p}) = \langle\Phi^-_{\boldsymbol{p}}|\Psi(t=\infty)\rangle, \tag{28}$$

where the continuum state $\Phi^-_{\boldsymbol{p}}$ is the outgoing asymptotic Coulomb wave function satisfying the following equation:

$$\left[-\frac{1}{2}\nabla^2+V(r)\right]\Phi^-_{\boldsymbol{p}} = \frac{p^2}{2}\Phi^-_{\boldsymbol{p}}. \tag{29}$$

Indeed, by solving the TDSE one can obtain the most accurate numerical results provided that the calculations are practical. Unfortunately, the TDSE calculations require a large amount of computing time and are impractical for long pulses at high intensities, so that results can only be obtained for a restricted regime of laser parameters. In addition, the insight into physics is hidden even though the numerical solutions of TDSE can be obtained.

2.4. Standard potential scattering theory

The QRS model was first proposed for HATI[28] in which laser-induced elastic scattering of electron with the parent ion plays a decisive role.[29,59,60] In this section, we briefly summarize the standard potential scattering theory which has been well documented in the text books; see Refs. [61] and [62], for example.

The scattered wavefunction of an electron by a potential $V(\boldsymbol{r})$ satisfies the time-independent Schrödinger equation

$$[\nabla^2+k^2-U(\boldsymbol{r})]\psi(\boldsymbol{r}) = 0, \tag{30}$$

where $U(\boldsymbol{r}) = 2V(\boldsymbol{r})$ is the reduced potential and k is the momentum, related to the electron energy by $k=\sqrt{2E}$.

For a short-range potential which falls faster than r^{-2} as $r\to\infty$, the wavefunction of the scattered electron in the asymptotic region is given by

$$\psi^+(\boldsymbol{r})_{r\to\infty} = \frac{1}{(2\pi)^{3/2}}\left[\exp({\rm i}\boldsymbol{k}\cdot\boldsymbol{r})+f(\theta,\phi)\frac{\exp({\rm i}kr)}{r}\right], \tag{31}$$

where $f(\theta,\phi)$ is the scattering amplitude.

To get the scattering amplitude, we solve Eq. (30) by expanding the scattered wavefunction in partial waves

$$\psi^{+}(\boldsymbol{r}) = \sqrt{\frac{2}{\pi}}\frac{1}{kr}\sum_{lm} \mathrm{i}^{l} u_l(k,r) Y_{lm}(\hat{\boldsymbol{r}}) Y^{*}_{lm}(\hat{\boldsymbol{k}}), \tag{32}$$

where Y_{lm} is a spherical harmonic. We take the convention that all continuum waves are normalized to $\delta(\boldsymbol{k}-\boldsymbol{k}')$. The radial equation that $u_l(k,r)$ satisfies can be obtained from Eq. (30) as

$$\left[\frac{\mathrm{d}^2}{\mathrm{d}r^2} + k^2 - \frac{l(l+1)}{r^2} - U(r)\right] u_l(k,r) = 0. \tag{33}$$

Here, we assume that the potential is radially symmetric, i.e., $V(\boldsymbol{r}) = V(r)$.

For a plane wave when $V(r) = 0$, the radial component $u_l(k,r)/kr$ in Eq. (32) is a standard spherical Bessel function $j_l(kr)$.

When $r \to \infty$, the boundary condition satisfied by $u_l(k,r)$ for $V(r) = 0$ is

$$u_l(k,r) = \sin\left(kr - \frac{1}{2}l\pi\right), \tag{34}$$

while for a short-range potential $V(r)$,

$$u_l(k,r) = \mathrm{e}^{\mathrm{i}\delta_l} \sin\left(kr - \frac{1}{2}l\pi + \delta_l\right). \tag{35}$$

From Eqs. (34) and (35) we see that it is the quantity δ_l, called the phase shift, that displays the influence of the interaction.

By matching the coefficients of the outgoing spherical waves in Eqs. (32) and (31), and using Eqs. (34) and (35), one finds that the scattering amplitude is independent of ϕ and given by

$$f(\theta) = \sum_{l=0}^{\infty} \frac{2l+1}{k} \exp(\mathrm{i}\delta_l) \sin\delta_l P_l(\cos\theta), \tag{36}$$

where $P_l(\cos\theta)$ are the Legendre polynomials.

For the scattering by a pure Coulomb potential

$$V_{\mathrm{c}}(r) = \frac{Z_1 Z_2}{r}, \tag{37}$$

where Z_1 and Z_2 are the charges of the projectile and the target, respectively, the method of partial waves is of little interest, since the Coulomb interaction drops off so slowly for large r. Fortunately, it can be treated in parabolic coordinates and the scattering amplitude can be obtained analytically

$$f_c(\theta) = -\eta \exp(2\mathrm{i}\sigma_0) \frac{\exp\{-\mathrm{i}\eta \ln[\sin^2(\theta/2)]\}}{2k\sin^2(\theta/2)}, \tag{38}$$

where

$$\sigma_0 = \arg[\Gamma(1+\mathrm{i}\eta)], \quad \eta = Z_1 Z_2/k. \tag{39}$$

However, for a real situation frequently encountered in electron scattering in which a short-range potential $V(r)$ is added to a pure Coulomb potential $V_{\mathrm{c}}(r)$ due to decreasing screening of the nucleus of the target ion by its electrons, one still needs to resort to the partial wave decomposition. Similarly, we expand the wavefunction as

$$\psi_{\mathrm{c}}^{+}(\boldsymbol{r}) = \sqrt{\frac{2}{\pi}}\frac{1}{kr}\sum_{lm} \mathrm{i}^{l}\, \mathrm{e}^{\mathrm{i}\sigma_l} u_l^{\mathrm{c}}(k,r) Y_{lm}(\hat{\boldsymbol{r}}) Y^{*}_{lm}(\hat{\boldsymbol{k}}), \tag{40}$$

and find that the radial wave equation for $u_l^{\mathrm{c}}(k,r)$ reads

$$\left[\frac{\mathrm{d}^2}{\mathrm{d}r^2} + k^2 - \frac{l(l+1)}{r^2} - U(r) - \frac{2\eta k}{r}\right] u_l^{\mathrm{c}}(k,r) = 0, \tag{41}$$

where the quantity

$$\sigma_l = \arg[\Gamma(l+1+\mathrm{i}\eta)] \tag{42}$$

is called the Coulomb phase shift. The asymptotic boundary condition satisfied by the scattered wavefunction $\psi_{\mathrm{c}}^{+}(\boldsymbol{r})$ is

$$\begin{aligned}&\psi_{\mathrm{c}}^{+}(\boldsymbol{r})_{r\to\infty}\\ &= \frac{1}{(2\pi)^{3/2}}\left\{\phi_{\mathrm{c}}(\boldsymbol{r}) + \hat{f}(\theta,\phi)\frac{\exp[\mathrm{i}(kr - \eta\ln 2kr)]}{r}\right\}.\end{aligned} \tag{43}$$

Here, $\phi_{\mathrm{c}}(\boldsymbol{r})$ is the Coulomb wavefunction given by

$$\begin{aligned}\phi_{\mathrm{c}}(\boldsymbol{r}) \;=\; &\exp\left(-\frac{1}{2}\pi\eta\right)\Gamma(1+\mathrm{i}\eta)\exp(\mathrm{i}\boldsymbol{k}\cdot\boldsymbol{r})\\ &\times {}_1F_1[-\mathrm{i}\eta; 1; \mathrm{i}(kr - \boldsymbol{k}\cdot\boldsymbol{r})].\end{aligned} \tag{44}$$

The boundary condition satisfied by $u_l^{\mathrm{c}}(k,r)$ when $r \to \infty$ is

$$u_l^{\mathrm{c}}(k,r) = \mathrm{e}^{\mathrm{i}\delta_l} \sin\left(kr - \frac{1}{2}l\pi + \eta\ln 2kr + \sigma_l + \delta_l\right). \tag{45}$$

Again, the phase shift δ_l is due to the short-range interaction $V(r)$. Similarly, the scattering amplitude $\hat{f}(\theta,\phi)$ in Eq. (43) can be obtained by matching the coefficients of the outgoing spherical waves in Eqs. (40) and (43) with the help of Eq. (45)

$$\hat{f}(\theta) = \sum_{l=0}^{\infty} \frac{2l+1}{k} \exp(2\mathrm{i}\sigma_l) \exp(\mathrm{i}\delta_l) \sin\delta_l P_l(\cos\theta). \tag{46}$$

Therefor, the scattering amplitude for the general case is given by

$$f(\theta) = f_{\mathrm{c}}(\theta) + \hat{f}(\theta), \tag{47}$$

and the elastic scattering DCS for a given incident energy reads

$$\frac{\mathrm{d}\sigma_{\mathrm{el}}}{\mathrm{d}\Omega} = |f(\theta)|^2. \tag{48}$$

2.5. Theoretical model for electron impact excitation

Laser-induced electron impact excitation is one of the main mechanisms in NSDI. To simulate the correlated two-electron momentum distributions based on the QRS model, one needs to calculate the DCSs for electron impact excitation of parent ions.

The distorted-wave Born approximation (DWBA) is one of most efficient methods dealing with inelastic collision processes. In this section, we briefly review the DWBA method for electron impact excitation of singly charged ion.

Suppose we have an electron with momentum $\boldsymbol{k}_i$ which collides with an atomic ion A^+, after the collision, the scattered electron has momentum $\boldsymbol{k}_f$, and one bound electron in the ground state is promoted to an excited state (nl). In the frozen core approximation, the exact Hamiltonian for the whole system is given by

$$H = -\frac{1}{2}\nabla_1^2 + V_{A^{2+}}(r_2) - \frac{1}{2}\nabla_2^2 + V_{A^{2+}}(r_1) + \frac{1}{|\boldsymbol{r}_1 - \boldsymbol{r}_2|}, \quad (49)$$

where $\boldsymbol{r}_1$ and $\boldsymbol{r}_2$ are the position vectors for the projectile and the bound state electron with respect to the nucleus, respectively, and $V_{A^{2+}}$ is the effective potential based on the single active electron approximation.

Both the exact initial state wavefunction $\Psi_i(\boldsymbol{r}_1, \boldsymbol{r}_2)$ and the final state wavefunction $\Psi_f(\boldsymbol{r}_1, \boldsymbol{r}_2)$ of the system satisfy the Schrödinger equation

$$H\Psi_j(\boldsymbol{r}_1, \boldsymbol{r}_2) = E\Psi_j(\boldsymbol{r}_1, \boldsymbol{r}_2), \quad (j = i, f), \quad (50)$$

where E is the total energy of the system. Since equation (50) cannot be solved analytically, we form approximate Hamiltonians, which can be expressed as

$$H_j = -\frac{1}{2}\nabla_1^2 + U_j(r_1) - \frac{1}{2}\nabla_2^2 + V_{A^{2+}}(r_2), \quad (j = i, f), \quad (51)$$

where U_i (U_f) is the distorting potential used to calculate the wavefunction $\chi_{\boldsymbol{k}_i}$ ($\chi_{\boldsymbol{k}_f}$) for the projectile in the incident (exit) channel with momentum $\boldsymbol{k}_i$ ($\boldsymbol{k}_f$). With this approximation, the initial (final) state wavefunction can be expressed as a product of the initial (final) state wavefunction for the projectile and the wavefunction for the bound electron in the ground (excited) state.

The wavefunctions for the electron in both initial ground state $\Phi_i(\boldsymbol{r}_2)$ and final excited state $\Phi_f(\boldsymbol{r}_2)$ satisfy the differential equation

$$\left[-\frac{1}{2}\nabla_2^2 + V_{A^{2+}}(r_2)\right]\Phi_j(\boldsymbol{r}_2) = \varepsilon_j\Phi_j(\boldsymbol{r}_2), \quad (j = i, f), \quad (52)$$

where ε_j $(j = i, f)$ are the corresponding eigenenergies of the initial and final states. The wavefunctions for the projectile in the initial and final states can be obtained by solving the following equation:

$$\left[-\frac{1}{2}\nabla_1^2 + U_j(r_1)\right]\chi_{\boldsymbol{k}_j}(\boldsymbol{r}_1) = \frac{1}{2}k_j^2\chi_{\boldsymbol{k}_j}(\boldsymbol{r}_1), \quad (j = i, f). \quad (53)$$

Due to the energy conservation, we have

$$\frac{1}{2}k_i^2 + \varepsilon_i = \frac{1}{2}k_f^2 + \varepsilon_f = E. \quad (54)$$

The distorting potentials U_i and U_f used in Eq. (53) play an important role in the numerical calculations, since the calculated DCSs are sensitive to the distorted wavefunctions describing the projectile. Unfortunately, neither U_i nor U_f is determined directly by the formalism. Here, we use the static potentials which are obtained by averaging over the motion of the active electron

$$U_j(r_1) = V_{A^{2+}}(r_1) + \int \mathrm{d}\boldsymbol{r}_2 \frac{|\Phi_j(\boldsymbol{r}_2)|^2}{|\boldsymbol{r}_1 - \boldsymbol{r}_2|}, \quad (j = i, f). \quad (55)$$

Obviously, the distorting potentials given by Eq. (55) for electron impact excitation of singly charged ion are Coulomb potential asymptotically.

In DWBA, the direct transition amplitude for excitation from an initial state Φ_i to a final state Φ_f is given by

$$f_{\mathrm{exc}} = \langle\chi^-_{\boldsymbol{k}_f}(\boldsymbol{r}_1)\Phi_f(\boldsymbol{r}_2)|V_{\mathrm{i}}|\Phi_i(\boldsymbol{r}_2)\chi^+_{\boldsymbol{k}_i}(\boldsymbol{r}_1)\rangle, \quad (56)$$

where V_{i} is the perturbation interaction

$$V_{\mathrm{i}} = H - H_{\mathrm{i}} = \frac{1}{r_{12}} + V_{A^{2+}}(r_1) - U_i(r_1). \quad (57)$$

And the exchange scattering amplitude is given by

$$g_{\mathrm{exc}} = \langle\Phi_f(\boldsymbol{r}_1)\chi^-_{\boldsymbol{k}_f}(\boldsymbol{r}_2)|V_{\mathrm{i}}|\Phi_i(\boldsymbol{r}_2)\chi^+_{\boldsymbol{k}_i}(\boldsymbol{r}_1)\rangle. \quad (58)$$

To evaluate the scattering amplitude, we perform the standard partial wave expansions. The details of numerical calculations for the scattering amplitude have been presented in Ref. [63]. Finally, the spin-averaged differential cross section for electron impact excitation from (N_i, L_i) to (N_f, L_f) is given by

$$\frac{\mathrm{d}\sigma_{\mathrm{exc}}}{\mathrm{d}\Omega} = N(2\pi)^4\frac{k_f}{k_i}\frac{1}{2L_i+1} \times \sum_{M_i=-L_i}^{+L_i}\sum_{M_f=-L_f}^{+L_f}\left(\frac{3}{4}|f_{\mathrm{exc}} - g_{\mathrm{exc}}|^2 + \frac{1}{4}|f_{\mathrm{exc}} + g_{\mathrm{exc}}|^2\right), \quad (59)$$

where the prefactor N denotes the number of electrons in the subshell from which one electron is excited.

The DWBA is a relatively simple model with respect to other sophisticated theoretical models, such as R-matrix method[64] and convergent close-coupling (CCC) approach.[65] For the calculations of correlated two-electron momentum distributions of NSDI at high laser intensities, the DWBA model is a good candidate since it can be calculated very quickly. Furthermore, the main important physics has been considered in DWBA such that the shape of the DCS is typically in fairly good agreement with the experimental measurements. However, it is well known that, at low energies,

the total cross sections (TCS) predicted by the DWBA significantly exceed the experimental values, especially at energies near the threshold, which implies that the DCSs of DWBA are also larger than the absolute experimental data. This suggests that the DCSs of DWBA at low energies require a special treatment before they are used to simulate the parallel momentum distributions for the returning electron after recollisional excitation of the parent ion. This special treatment has been accomplished by introducing a calibration procedure for DWBA.[66]

2.6. Theoretical model for electron impact ionization

Now we consider electron impact ionization which is another dominant mechanism in NSDI. Different from the process of electron impact excitation, in $(e, 2e)$ process, there are two outgoing electrons. Suppose we have an electron with momentum $\boldsymbol{k}_i$ which collides with a singly charged ion in its ground state; after the collision two outgoing electrons with momentum $\boldsymbol{k}_1$ and $\boldsymbol{k}_2$ are detected in coincidence. For this process, the triple differential cross section (TDCS) is given by

$$\frac{\mathrm{d}^3\sigma_{e2e}}{\mathrm{d}\Omega_1\mathrm{d}\Omega_2\mathrm{d}E_2} = (2\pi)^4\frac{k_1k_2}{k_i}\left[\frac{3}{4}|f_{e2e}(\boldsymbol{k}_1,\boldsymbol{k}_2)-f_{e2e}(\boldsymbol{k}_2,\boldsymbol{k}_1)|^2 + \frac{1}{4}|f_{e2e}(\boldsymbol{k}_1,\boldsymbol{k}_2)+f_{e2e}(\boldsymbol{k}_2,\boldsymbol{k}_1)|^2\right], \quad (60)$$

where $\Omega_1(\theta_1,\phi_1)$ and $\Omega_2(\theta_2,\phi_2)$ are the solid angles of detectors for the two electrons leaving the collision along $\hat{\boldsymbol{k}}_1$ and $\hat{\boldsymbol{k}}_2$, and $f_{e2e}(\boldsymbol{k}_1,\boldsymbol{k}_2)$ and $f_{e2e}(\boldsymbol{k}_2,\boldsymbol{k}_1)$ are the transition amplitudes for the direct and exchange processes, respectively. In the prior form, the direct transition amplitude of the $(e, 2e)$ process is expressed by

$$f_{e2e}(\boldsymbol{k}_1,\boldsymbol{k}_2) = \langle\Psi^-_{\boldsymbol{k}_1,\boldsymbol{k}_2}(\boldsymbol{r}_1,\boldsymbol{r}_2)|V_\mathrm{i}|\Psi^+_{\boldsymbol{k}_i}(\boldsymbol{r}_1,\boldsymbol{r}_2)\rangle, \quad (61)$$

where V_i is the perturbation interaction given in Eq. (57), and $\boldsymbol{r}_1$ and $\boldsymbol{r}_2$ are the position vectors of the projectile and the bound state electron, respectively, with respect to the target nucleus.

2.6.1. The DWBA model

Similar to electron impact excitation, the transition amplitude for the $(e, 2e)$ process can also be evaluated by using the DWBA model. The initial state wavefunction is exactly the same as that for electron impact excitation, i.e.,

$$\Psi^+_{\boldsymbol{k}_i}(\boldsymbol{r}_1,\boldsymbol{r}_2) = \Phi_i(\boldsymbol{r}_2)\chi^+_{\boldsymbol{k}_i}(\boldsymbol{r}_1). \quad (62)$$

In DWBA, the asymptotic final state wavefunction for the two outgoing electrons is expressed as

$$\Psi^-_{\boldsymbol{k}_1,\boldsymbol{k}_2}(\boldsymbol{r}_1,\boldsymbol{r}_2) = \chi^-_{\boldsymbol{k}_1}(\boldsymbol{r}_1)\chi^-_{\boldsymbol{k}_2}(\boldsymbol{r}_2). \quad (63)$$

The wavefunctions for the two outgoing electrons satisfy the following equations:

$$\left[-\frac{1}{2}\nabla_1^2+U_f(r_1)\right]\chi_{\boldsymbol{k}_1}(\boldsymbol{r}_1) = \frac{1}{2}k_1^2\chi_{\boldsymbol{k}_1}(\boldsymbol{r}_1), \quad (64)$$

$$\left[-\frac{1}{2}\nabla_2^2+V_{A^{2+}}(r_2)\right]\chi_{\boldsymbol{k}_2}(\boldsymbol{r}_2) = \frac{1}{2}k_2^2\chi_{\boldsymbol{k}_2}(\boldsymbol{r}_2). \quad (65)$$

Due to the energy conservation, we have

$$\frac{1}{2}k_i^2 = \frac{1}{2}k_1^2+\frac{1}{2}k_f^2+I_\mathrm{p}. \quad (66)$$

The standard partial wave expansions are also made to evaluate the scattering amplitude for $(e, 2e)$. For details, see Ref. [67].

Again, the DWBA model for $(e, 2e)$ is also only valid at high impact energies since the final-state electron–electron interaction, which is important in the collision process at intermediate and low energies, has not been taken into account. The group of Madison has improved the DWBA model by including the final-state Coulomb interaction directly in the final-state wavefunction.[68,69] It has been found that, for intermediate energies, the post-collision interaction between the two outgoing electrons has an important effect and leads to an overall improvement in the agreement between experiment and theory.

2.6.2. The BBK model

For electron impact ionization of He^+ ion, the final-state electron–electron interaction has been taken into account in the Brauner, Briggs, and Klar (BBK) model[70] in which an approximate three-body scattering wavefunction for the final state that satisfies the asymptotic three-body Schrödinger equation (50) exactly was derived analytically. The BBK wavefunction consists of a product of three Coulomb (3C) wavefunctions which is expressed as

$$\begin{aligned}&\Psi^-_{\boldsymbol{k}_1,\boldsymbol{k}_2}(\boldsymbol{r}_1,\boldsymbol{r}_2)\\ &= (2\pi)^{-3}\exp(\mathrm{i}\boldsymbol{k}_1\cdot\boldsymbol{r}_1)\exp(\mathrm{i}\boldsymbol{k}_2\cdot\boldsymbol{r}_2)C(\alpha_1,\boldsymbol{k}_1,\boldsymbol{r}_1)\\ &\times C(\alpha_2,\boldsymbol{k}_2,\boldsymbol{r}_2)C(\alpha_{12},\boldsymbol{k}_{12},\boldsymbol{r}_{12}),\end{aligned} \quad (67)$$

where the Coulomb part of the wavefunction is defined as

$$C(\alpha,\boldsymbol{k},\boldsymbol{r}) = \mathrm{e}^{-\pi\alpha/2}\Gamma(1-\mathrm{i}\alpha)_1F_1[\mathrm{i}\alpha;1;-\mathrm{i}(kr+\boldsymbol{k}\cdot\boldsymbol{r})], \quad (68)$$

with

$$\boldsymbol{k}_{12} = \frac{1}{2}(\boldsymbol{k}_1-\boldsymbol{k}_2),\quad \boldsymbol{r}_{12} = \boldsymbol{r}_1-\boldsymbol{r}_2,$$
$$\alpha_1 = -\frac{Z_N}{k_1},\quad \alpha_2 = -\frac{Z_N}{k_2},\quad \alpha_{12} = \frac{1}{2k_{12}}. \quad (69)$$

In Eq. (68), Γ is the gamma function and ${}_1F_1$ is the confluent hypergeometric function. If $1/|\boldsymbol{r}_1-\boldsymbol{r}_2|$ is dropped in Eq. (49), the interaction between the two outgoing electrons is turned off. Consequently, the final-state wavefunction becomes a product of two Coulomb (2C) wavefunctions by setting $\alpha_{12} = 0$ in Eq. (67). It should be noted that the 2C

wavefunction, which is equivalent to the asymptotic final state wavefunction in DWBA if the distortion of the short range potential is neglected, does not satisfy the proper asymptotic three-body boundary condition.

In the BBK model which was originally proposed for the process of electron impact ionization of hydrogen, a plane wave is used to describe the incoming electron since the target is neutral. However, for electron impact ionization of He^+ ion, a Coulomb wave should be employed to account for the Coulomb attraction between the incident electron and the target ion. The Coulomb wavefunction for the incident electron takes the form

$$\chi^+_{\boldsymbol{k}_i}(\boldsymbol{r}_1) = \frac{1}{(2\pi)^{3/2}}\exp(-\pi\alpha_i/2)\Gamma(1+\mathrm{i}\alpha_i) \times \exp(\mathrm{i}\boldsymbol{k}_i\cdot\boldsymbol{r}_1)\,{}_1F_1[-\mathrm{i}\alpha_i;1;i(k_i r_1-\boldsymbol{k}_i\cdot\boldsymbol{r}_1)], \quad (70)$$

where $\alpha_i=-1/k_i$. In this case, the transition amplitude involves four Coulomb (4C) wavefunctions. With the precollision interaction between the incident electron and the target ion taken into account, Jia *et al.*[71] first carried out the numerical calculations of TDCS for electron impact ionization of He^+ ion at intermediate impact energies.

It should be mentioned that some deficiencies still exist in the BBK wavefunction although it satisfies the asymptotic three-body Schrödinger equation exactly. The major limitation of the 3C wave function lies in the fact that the influence on the strength of the interaction of any two particles by the presence of a third one has not been taken into account. This deficiency was first corrected for the case in which the two outgoing electrons have equal energies by introducing effective Sommerfeld parameters,[72] and was later generalized for any energy sharing in all geometries.[73] Such a modification reflects the dynamic screening of the three-body Coulomb interactions.

2.7. Focal volume averaging

Numerical simulations for spectra are usually performed for a single laser intensity. However, when atoms are exposed to a laser field, they experience different intensities across the beam profile. For a Gaussian beam, the intensity distribution is given by

$$I(\rho,z)=I_0\frac{w_0^2}{w^2(z)}\exp\left[-\frac{2\rho^2}{w^2(z)}\right], \quad (71)$$

where

$$w(z)=w_0[1+(z/z_0)^2]^{1/2}, \quad (72)$$

and $w_0=\sqrt{\lambda z_0/\pi}$ denotes the Rayleigh range of the focus.

Since experiment collects electrons originating from atoms located anywhere in the interaction volume, direct comparison of the experimental data with the theoretical spectra is acceptable only when the focal volume effect has been taken into account. Therefore, integration over the focus volume should be performed by finding the volume of each isointensity shell. For example, the focal volume averaged total yield of single ionization at a peak intensity I_0 can be obtained by

$$\bar{Y}^+=\int Y^+(I(\rho,z))\mathrm{d}V=\int_0^{I_0}Y^+(I)\frac{\partial V}{\partial I}\mathrm{d}I, \quad (73)$$

where the volume of an isointensity shell between I and $I+\mathrm{d}I$ is given by[74]

$$\frac{\partial V}{\partial I}\mathrm{d}I = \pi z_0 w_0^2\left\{\frac{4(c_1-c_2)}{3}+\frac{2(c_1^3-c_2^3)}{9} -\frac{4}{3}\left[\tan^{-1}(c_1)-\tan^{-1}(c_2)\right]\right\}, \quad (74)$$

with $c_1=[(I_0-I)/I]^{1/2}$ and $c_2=\{[I_0-(I+\mathrm{d}I)]/(I+\mathrm{d}I)\}^{1/2}$.

3. The quantitative rescattering model

Laser-induced rescattering processes have been well understood based on the three-step classical rescattering model.[6,22] In the first step, the electron tunnels out from an atom. In the second step, the electron moves in the laser field and returns to the parent core. Finally, in the third step, the electron collides with the parent ion. During the collision, both elastic and inelastic scatterings could take place. The elastic scattering of the returning electron with the parent ion leads to HTAI,[75] and the recombination of the returning electron with the parent ion produces HHG.[76] On the other hand, NSDI[77] is due to inelastic scattering of the returning electron by the parent ion, in which two mechanisms could be involved, one is the direct ionization of the parent and the other one is recollision excitation with subsequent ionization. In the simulation of all the laser-induced rescattering processes, the RWP which describes the momentum distribution of the returning electron plays a significantly important role.

3.1. Returning electron wave packet

According to the QRS model, the momentum distribution of the HATI photoelectron with momentum $\boldsymbol{p}$ is expressed as a product of the RWP and the DCS for elastic scattering of the returning electron with the parent ion.[28,29] By defining

$$D^{\mathrm{HATI}}_{\mathrm{SFA}}(\boldsymbol{p})\equiv\frac{\mathrm{d}^3P_{\mathrm{SFA}}}{\mathrm{d}p_x\mathrm{d}p_y\mathrm{d}p_z}=|f^{(2)}_{\mathrm{SFA}}(\boldsymbol{p})|^2, \quad (75)$$

the QRS model for HATI reads

$$D^{\mathrm{HATI}}_{\mathrm{SFA}}(\boldsymbol{p})=W_{\mathrm{SFA}}(k_r)\frac{\mathrm{d}\sigma^{\mathrm{el}}_{\mathrm{PWBA}}(k_r,\theta_r)}{\mathrm{d}\Omega_r}, \quad (76)$$

where $W(k_r)$ is the RWP describing the momentum distribution of the returning electrons, and $\mathrm{d}\sigma^{\mathrm{el}}_{\mathrm{PWBA}}(k_r,\theta_r)/\mathrm{d}\Omega_r$ is the DCS, calculated within the plane wave first-order Born approximation (PWBA), for an electron with a momentum of magnitude k_r to be scattered at an angle θ_r with respect to the direction of the returning electron.

The detected photoelectron momentum $\boldsymbol{p}$ and the momentum $\boldsymbol{k}_r$ of the scattered electron are related by[28]

$$\boldsymbol{p} = \boldsymbol{k}_r - \boldsymbol{A}_r, \tag{77}$$

with

$$k_r = 1.26|A_r|, \tag{78}$$

where $\boldsymbol{A}_r \equiv \boldsymbol{A}(t_r)$ is the instantaneous vector potential at the returning time t_r when the recollision takes place. It should be noted that the relation between k_r and $|A_r|$ is determined approximately by solving the Newton's equation of motion for an electron in a monochromatic laser field.[28] Equation (78) is an inherent approximation used in the QRS theory but the error is insignificant. This issue has been discussed in detail in Ref. [28] in which the validity of the QRS model for HATI has also been extensively verified.

The RWP is then obtained by

$$W_{\rm SFA}(k_r) = D^{\rm HATI}_{\rm SFA}(\boldsymbol{p}) \Big/ \frac{{\rm d}\sigma^{\rm el}_{\rm PWBA}(k_r,\theta_r)}{{\rm d}\Omega_r}. \tag{79}$$

It has been established[28] that, equation (76) also holds for the HATI photoelectron spectra from the TDSE if the DCS for elastic scattering of electron with the parent ion is calculated based on the standard potential scattering theory. This indicates that the RWP can also be obtained from solving the TDSE, i.e.,

$$W_{\rm TDSE}(k_r) = D^{\rm HATI}_{\rm TDSE}(\boldsymbol{p}) \Big/ \frac{{\rm d}\sigma^{\rm el}(k_r,\theta_r)}{{\rm d}\Omega_r}, \tag{80}$$

where

$$D^{\rm HATI}_{\rm TDSE}(\boldsymbol{p}) = |f_{\rm TDSE}(\boldsymbol{p})|^2. \tag{81}$$

Figure 1 shows the RWPs extracted from the HATI photoelectron momentum distributions, calculated by solving the TDSE and using the SFA2, for Ar in 5 fs laser pulses with the wavelength of 800 nm at the intensities of 1.0×10^{14} W/cm^2 and 2.0×10^{14} W/cm^2, respectively. One can see that the RWP from SFA2 bears a striking resemblance to that from TDSE. Figure 1 also demonstrates that, the RWPs from both SFA2 and TDSE exhibit no dependence on the rescattering angle θ_r. This property indicates that one only needs to calculate the RWP at an arbitrary rescattering angle. In the real calculations, usually a large scattering angle, say $\theta_r = 170^\circ$, is chosen.

Another important property of the RWP is that it is almost independent of the target. Figure 2 displays the RWPs from SFA2 for single ionization of H and Ar in 5-cycle pulses at the intensity of 1.0×10^{14} W/cm^2 with the wavelength of 800 nm and the intensity of 0.8×10^{14} W/cm^2 with the wavelength of 2000 nm, respectively. Due to the reason stated above, in Fig. 2 the RWPs are extracted from the HATI photoelectron momentum distributions along a fixed outgoing angle θ, which has a one-to-one relation with the rescattering angle θ_r, and plotted as a function of only the momentum of the returning electron. It can be seen that the RWPs shown in Fig. 2(a) are quite different from those in Fig. 2(b). However, the RWP for H is almost the same as that for Ar for a given laser pulse. This indicates that the RWP depends only on the laser parameters but not on the target. It is well known that the information of both the laser parameters and the atomic structure is imprinted in the HATI photoelectron momentum spectra. Nevertheless, since the RWP only depends on the laser field and the DCS is totally determined by the target, the QRS model, as it is expressed by Eq. (75), can be used to extract the information of the target structure from the HATI photoelectron momentum spectra measured in experiment.[78–80]

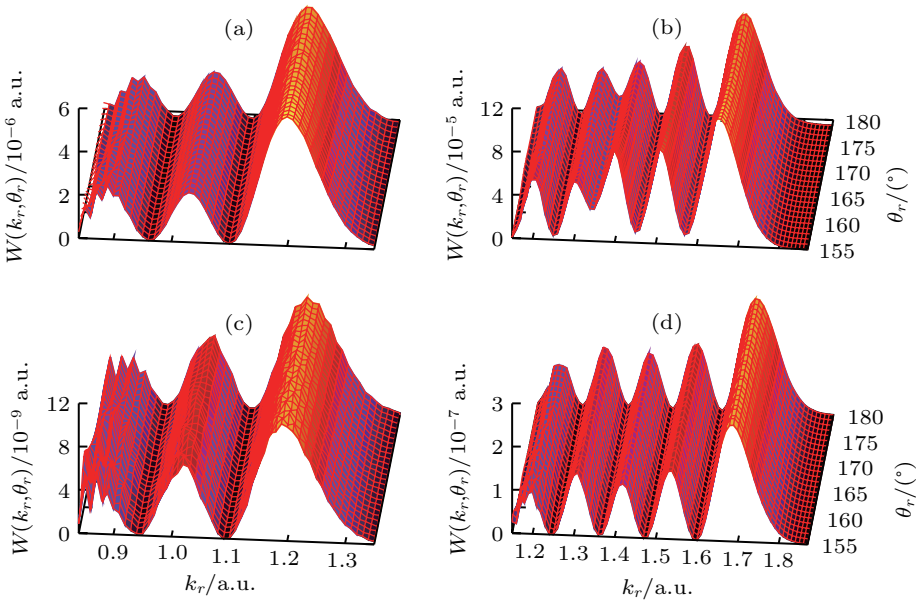


Fig. 1. Right-side wave packets ($p_z > 0$) extracted from the TDSE and SFA2 electron momentum distributions for single ionization of Ar in a 5 fs laser pulse with the wavelength of 800 nm. (a), (c) TDSE and SFA2 results at the intensity of 1.0×10^{14} W/cm^2; (b), (d) TDSE and SFA2 results at the intensity of 2.0×10^{14} W/cm^2. Adapted from Ref. [28].

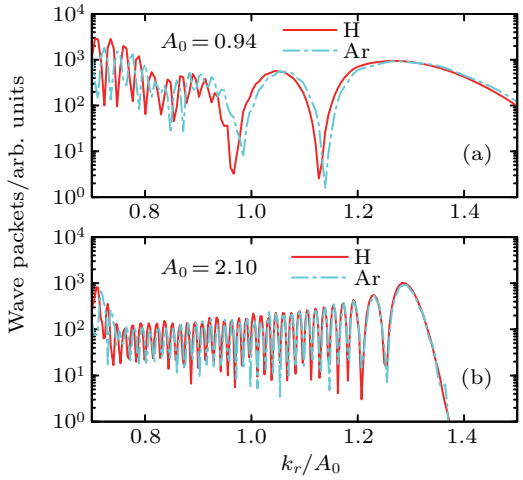


Fig. 2. Right-side wave packets extracted from SFA2 for single ionization of H and Ar in a 5-cycle laser pulse at (a) the intensity of 1.0×10^{14} W/cm^2 with the wavelength of 800 nm, and (b) the intensity of 0.8×10^{14} W/cm^2 with the wavelength of 2000 nm. Adapted from Ref. [28].

3.2. Total yield of doubly charged ion

The QRS model for NSDI was first applied to the calculations of the total yield of doubly charged ion.[30] The total yield of doubly ionization due to NSDI in a linearly polarized laser pulse at a single peak intensity I can be expressed by

$$\mathcal{Y}^{2+}(I) = \int \mathrm{d}E_r[W_{\mathrm{L}}(E_r)+W_{\mathrm{R}}(E_r)] \times[\sigma_{\mathrm{exc}}(E_r)+\sigma_{e2e}(E_r)], \quad (82)$$

where $E_r = k_r^2/2$ is the energy of the returning electron, $\sigma_{\mathrm{exc}}(E_r)$ and $\sigma_{e2e}(E_r)$ are the TCSs for electron impact excitation and ionization from the ground state of the target ion, and $W_{\mathrm{L}}(E_r)$ and $W_{\mathrm{R}}(E_r)$ are the returning electron wave packets extracted from the "left" ($p_z<0$) and the "right" ($p_z>0$) sides of the 2D momentum distributions for the HATI photoelectrons, respectively. For long pulses considered here, $W_{\mathrm{L}}(E_r) = W_{\mathrm{R}}(E_r)$.

As mentioned in Subsection 2.7, to compare with experiment, the focal volume effect has to be taken into account. However, since the total cross sections $\sigma_{\mathrm{exc}}(E_r)$ and $\sigma_{e2e}(E_r)$ in Eq. (82) do not depend on the laser parameters, the focal volume integral has only to be performed for the returning electron wave packets. Therefore, the total yield for the doubly charged ion at the peak intensity I_0 can be obtained by

$$\bar{\mathcal{Y}}^{2+}(I_0) = \int \mathrm{d}E_r[\bar{W}_{\mathrm{L}}(E_r)+\bar{W}_{\mathrm{R}}(E_r)] \times[\sigma_{\mathrm{exc}}(E_r)+\sigma_{e2e}(E_r)], \quad (83)$$

where $\bar{W}_j(E_r)$ $(j=\mathrm{L},\mathrm{R})$ are the focal volume averaged wave packets.

In Fig. 3, the simulated results by using Eq. (83) for the yields of doubly charged ions for NSDI of He in a linearly polarized laser pulse at 780 nm with the pulse duration of 120 fs[35] are compared with the experimental measurements of Walker *et al.*[5] In the numerical calculations, the returning electron wave packets and the total cross sections are evaluated by using the SFA2 and the R-matrix theory,[81] respectively. It can be seen from Fig. 3 that, while the model results are in good agreement with experiment in the regime of intermediate intensities, the QRS model fails to reproduce the total yield of doubly charged ion at both low and high intensities. This clearly indicates that the QRS model should be improved when it is applied to NSDI.

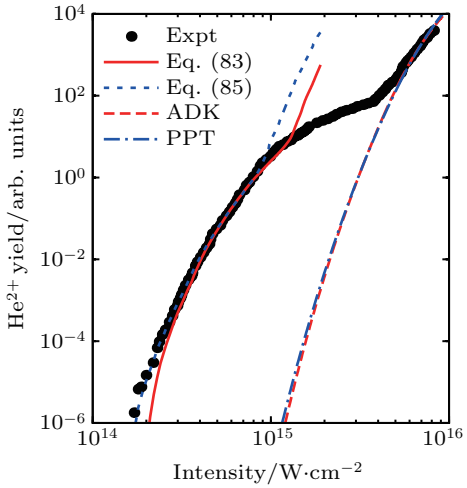


Fig. 3. Comparison of the simulated results for the yields of doubly charged ions with the experimental data for He in linearly polarized laser pulses at 780 nm. The solid circles represent the measurements of Walker *et al*,[5] while the dotted and solid curves are the QRS simulations with and without taking into account the shift of the continuum threshold energy due to the presence of an electric field at the collision time, respectively. The screening factor was set to $\alpha = 1.0$. The simulated results are relative and normalized to the experimental data individually at the intensity of 4.5×10^{14} W/cm^2. The curves on the right are the calculated sequential He^{2+} yields using ADK and PPT. Adapted from Ref. [35].

According to the classical rescattering model, the maximum kinetic energy that a returning electron can gain from the field is $3.17U_{\mathrm{p}}$, which is proportional to the laser intensity. This indicates that a minimum intensity, referred to as the threshold intensity, is required for the returning electron to have enough energy to ionize an electron of the residual ion or to promote this electron to an excited state. Nevertheless, this threshold intensity has never been observed in experiment.[82] van der Hart and Burnett[40] argued that the incorrect threshold intensity appears from the assumption in the recollision model that scattering can be treated as if it takes place in a free atom. As a matter of fact, this assumption is not true. In a free atom or ion, an incoming electron can promote the ground-state electron to an excited state and remain a continuum electron only when its kinetic energy is larger than the energy difference between the ground state and the excited state, since the total energy of a continuum electron must be positive. In contrast, in the case when the collision takes place in an electric field, the combined atomic and electric potentials form a barrier below zero. As a result, the projectile electron can escape from the atom or ion even with negative energy as long as its energy is higher than the potential barrier.[40]

Therefore, in the laser-induced recollision process, electron impact excitation of the parent ion can still take place even when the returning electron has an energy less than the energy difference between the ground state and the excited state. This phenomenon is usually referred to as "lowering of threshold". This does not mean, however, that the energy level of an excited state is lowered.

The maximum barrier height in the combined Coulomb and electric field potentials is given by[40]

$$V_{\rm b} = -2\sqrt{Z_{\rm eff}|F_r|}, \tag{84}$$

where $Z_{\rm eff}$ is the effective charge of the Coulomb potential seen by the projectile electron asymptotically, and F_r is the electric field at the instant of collision. For electron impact excitation and ionization of a singly-charged ion, $Z_{\rm eff} = 1$ and 2, respectively. Thus, for electron impact excitation and electron impact ionization taking place in an electric field, the threshold is lowered by $|V_{\rm b}|$.

Unfortunately, it is still a formidable task to perform actual numerical calculations with the lowering of threshold included. Alternatively, van der Hart and Burnett[40] suggested that, to account for the lowering of threshold, one should adjust the collision energy so that the returning electron energy E_r $(= E_i)$ corresponds to the incoming energy $E_r + |V_{\rm b}|$ for electron impact excitation and ionization in the field-free case. Based on these considerations, the QRS model could be improved, and thus equation (83) should be modified as

$$\begin{aligned}\bar{\mathcal{Y}}^{2+}(I_0) = & \int {\rm d}E_r[\bar{W}_{\rm L}(E_r) + \bar{W}_{\rm R}(E_r)] \\ & \times [\sigma_{\rm exc}(E_r + 2\sqrt{|F_r|}) \\ & + \sigma_{e2e}(E_r + 2\sqrt{2|F_r|})].\end{aligned} \tag{85}$$

Furthermore, since the barrier height of the combined atomic and electric field varies with the time when the laser-induced electron returns to the origin, an "average" returning time is chosen to make the calculations tractable. The method used to determine the average returning time was described in Ref. [37]. For example, by choosing an average returning time of $\omega t_r = 290^\circ$, one obtains the maximum shifts for the threshold energies of 21 eV and 15 eV, for ionization and excitation, respectively, at a laser peak intensity of 15×10^{14} W/cm^2.

As demonstrated in Fig. 3, by using Eq. (85) with the lowering of threshold taken into account, the improved QRS model successfully reproduced the the total yield of the doubly charged ion measured in experiment at low intensities. However, as also seen from Fig. 3, the threshold shift does not improve the model results at high intensities. In contrast, the agreement between the simulations and measurements at intensities above 9.0×10^{14} W/cm^2 becomes even worse. This deviation has been traced back to the returning electron wave packet in the region of low energy.[35]

As indicated in Subsection 2.2, a screening parameter α was introduced in Eq. (22) to avoid the singularity in the probability amplitude of SFA2. In Fig. 3, the parameter $\alpha = 1.0$ was used. It has already been recognized[20] that the HATI photoelectron energy spectra generated by SFA2 are sensitive to the screening factor at low energies (below $2U_{\rm p}$), but remain almost the same at high energies (above $4U_{\rm p}$). This is also true for the returning electron wave packets obtained from SFA2. Figure 4(a) shows how the RWP changes with the returning energy for $\alpha = 1.0$ at three peak laser intensities. One can see that each RWP starts with a fast drop at low energies before becoming flat in the plateau region, somewhat mimicking the HATI spectra. The disagreement between theory and experiment in the high-intensity region, shown in Fig. 3, originates from the large magnitude of the low-energy distribution in the RWP. When the excitation threshold is shifted down by the laser field, the low-energy part of the RWP contributes more to double ionization. That is why the simulated results deviate more from experiment when the lowering of threshold energy is included. The dependence of the RWP on the screening parameter is displayed in Fig. 4(b). As it is expected, the screening factor does not affect the RWP in the plateau region. On the contrary, in the low energy region, the RWP decreases substantially with the increase of the screening factor until $\alpha = 3$ when it is stabilized.

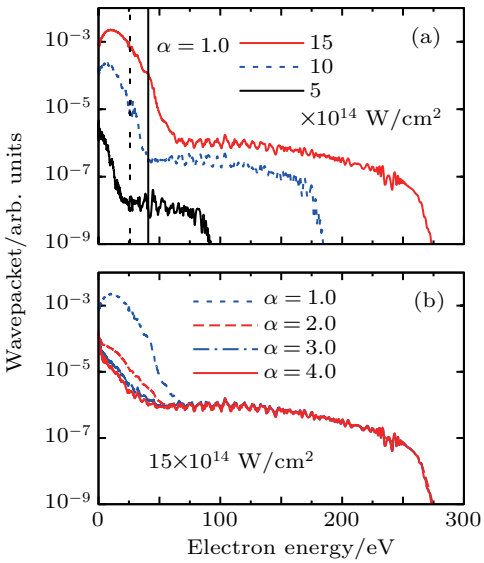


Fig. 4. Returning electron wave packets for He in linearly polarized laser pulses at 780 nm. (a) The screening factor is chosen as $\alpha = 1.0$, and the peak intensities are 5×10^{14} W/cm^2, 10×10^{14} W/cm^2, and 15×10^{14} W/cm^2, respectively. (b) The peak intensity is 15×10^{14} W/cm^2 and the screening factors are $\alpha = 1.0$, 2.0, 3.0, and 4.0, respectively. The calculations include integration over the laser focus volume. In panel (a), the vertical solid line marks the excitation threshold of He^+ in the field-free case, while the vertical dotted line marks the corresponding threshold for excitation in the field at a peak intensity of 15×10^{14} W/cm^2. Adapted from Ref. [35].

It is found that as α is increased, the model calculations converge to the experimental data, as demonstrated in Fig. 5. The inset of this figure depicts the ratio of ionization with re-

spect to excitation for the production of He^{2+} ions as a function of the peak laser intensity.

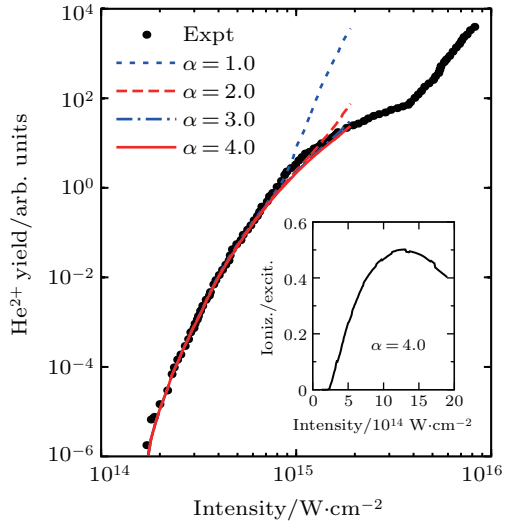


Fig. 5. Comparison of the simulated results, with the shift of the continuum threshold energy taken into account, for the yields of doubly charged ions with the experimental data for He in linearly polarized laser pulses at 780 nm. The solid circles represent the measurements of Walker *et al*,[5] while the lines are simulated results for $\alpha = 1.0$, 2.0, 3.0, and 4.0, respectively. The theoretical predictions are relative and were normalized to the experimental data at the peak intensity of 4.5×10^{14} W/cm^2 with a fixed factor for each screening factor. The inset shows the ratio of the contributions to double ionization from ionization and excitation. Adapted from Ref. [35].

It should be noted that, for He, singlet cross sections for both electron impact excitation and electron impact ionization of the parent ion should be used in the numerical simulations for NSDI, since the two electrons involved in the process start in the singlet ground state, and their singlet coupling is preserved during recollision. This effect is virtually absent in other noble gases with many valence electrons and hence spin-averaged cross sections should be used.

With the improved QRS model, Chen *et al*.[36] have also simulated the total yields of doubly charged ions for NSDI of He and Ne in intense laser pulses at wavelengths of 390 nm and 400 nm, respectively, and the obtained results are in very good agreement with the experimental data over a broad range of laser intensities.

3.3. Double-to-single ionization ratio

While double ionization yields versus laser intensity provide the first evidence that strong-field NSDI occurs in favor of the classical recollision model, the measured experimental data are relative. In contrast, the absolute values of the double-to-single ionization ratio can be determined in experiments and hence offer a more stringent test of the theoretical models. Theoretically, to simulate the double-to-single ionization ratio, one needs to obtain the absolute values for both double and single ionization yields.

In the previous section, the RWPs used in the simulations of the double ionization yield are evaluated by using SFA2. Nevertheless, it has been demonstrated[28] that the RWP of SFA2 only has the correct momentum or energy dependence but not the absolute value with respect to the RWP calculated by solving the TDSE. This might indicate that, in order to obtain the absolute total yield of doubly charged ion, one should use the RWP from TDSE. Unfortunately, the TDSE calculations are very time-consuming and very computationally demanding for long pulses at high intensities. Therefore, it is almost impossible to solve the TDSE for the simulations of real experiments, as for the situations considered here. However, since the only difference between the RWPs from SFA2 and TDSE, for a given laser pulse at a peak intensity I with a wavelength λ and a pulse duration Γ, is a normalization factor, it is still possible for one to obtain the correct absolute RWPs by renormalizing the RWP from SFA2 according to[38]

$$W_{\rm abs}(I,\lambda,\Gamma) = C(I,\lambda,\Gamma) \times W_{\rm SFA2}(I,\lambda,\Gamma), \tag{86}$$

where the normalization factor is given by

$$C(I,\lambda,\Gamma) = \frac{W_{\rm TDSE}(I,\lambda,\Gamma)}{W_{\rm SFA2}(I,\lambda,\Gamma)}. \tag{87}$$

Nevertheless, the above equations are essentially useless since they only mean that $W_{\rm abs}(I,\lambda,\Gamma) = W_{\rm TDSE}(I,\lambda,\Gamma)$. However, since the RWPs from SFA2 and TDSE should have the same pulse duration dependence, the normalization factor should not depend on the pulse duration significantly. Consequently, equation (87) can be approximately rewritten as

$$C(I,\lambda,\Gamma) \simeq C(I,\lambda,\Gamma') = \frac{W_{\rm TDSE}(I,\lambda,\Gamma')}{W_{\rm SFA2}(I,\lambda,\Gamma')}. \tag{88}$$

The great advantage of the above equation is that it allows one to choose a few-cycle short pulse in the actual calculations for the normalization factor.

To obtain the double-to-single ionization ratio, one also needs to evaluate the total single ionization yield. Several theoretical models, such as ADK, PPT, SFA, and TDSE, can be used to calculate the single ionization yield. All of these theoretical models, except TDSE, are not able to reproduce the correct absolute ionization yields despite that the general trend of the ionization yield as a function of laser intensity can be well predicted by PPT and SFA. Again, this indicates that one also needs to calibrate the PPT or SFA results. For single ionization, a similar procedure could be applied by using the ionization probability from solving the TDSE for a short pulse at low intensity to renormalize the ionization probability from PPT or SFA. Details of the TDSE calculations and the normalization procedure can be found in Refs. [38] and [55], respectively.

As an example, in Fig. 6 we show the comparison of the returning electron wave packets from TDSE and SFA2 for Ne in a linearly polarized 800 nm laser field as well as the ratio of the single ionization yield from TDSE over that of PPT. From Figs. 6(a)–6(c), one can see that, with appropriate rescaling factors, the RWPs of SFA are in very good agreement with

those of TDSE in the plateau region. In addition, it is demonstrated that the normalization factors for different pulse durations and different laser intensities are quite close, which confirms the assumption made in Eq. (88). It should be noted that in the low energy regime, the RWPs of TDSE are much higher than those of SFA2. This is due to the fact that the contributions from direct ionization and laser-induced rescattering cannot be separated in the TDSE photoelectron spectra below $2U_p$. Similarly, one can see from Fig. 6(d) that, the ratios of Y^+_{TDSE}/Y^+_{PPT} at different intensities are almost constant and very close to 1. This indicates that the PPT theory is a good candidate to evaluate the total single ionization yield, and the ratio of Y^+_{TDSE}/Y^+_{PPT} does not depend on the pulse duration and the laser intensity either.

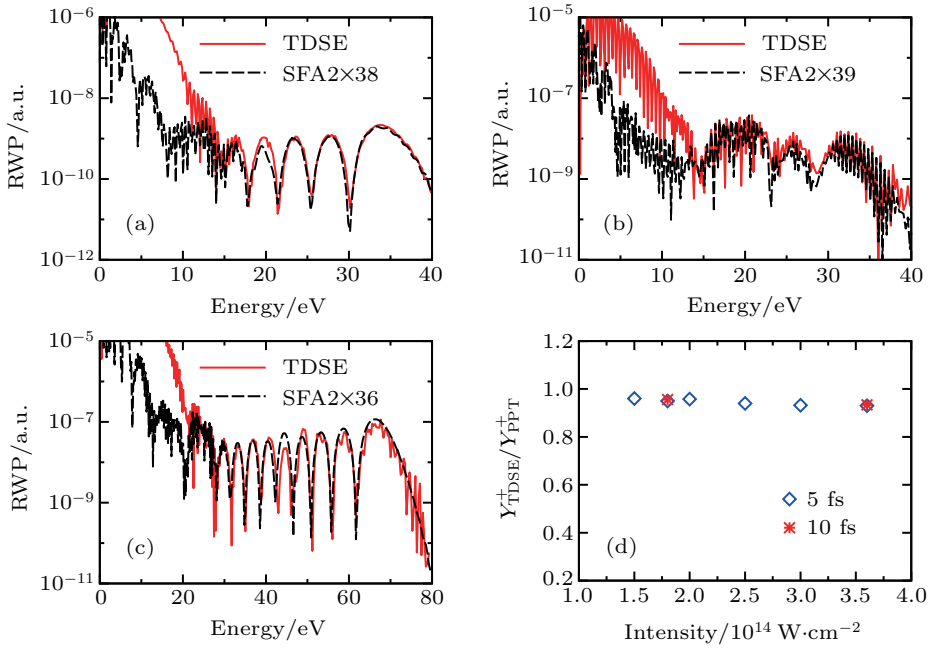


Fig. 6. Comparison of the returning electron wave packets from TDSE and SFA2 for Ne in a linearly polarized 800-nm laser field with parameters of (a) 5 fs and 1.8×10^{14} W/cm^2, (b) 10 fs and 1.8×10^{14} W/cm^2, and (c) 5 fs and 3.6×10^{14} W/cm^2. Panel (d) shows the ratio of the single ionization yield from TDSE (Y^+_{TDSE}) over the single ionization yield of PPT (Y^+_{PPT}) for Ne in a linearly polarized 800-nm laser field as a function of intensity for pulse durations of 5 fs and 10 fs, respectively. In (a)–(c), the returning electron wave packets of SFA2 are renormalized according to the corresponding TDSE results. Adapted from Ref. [38].

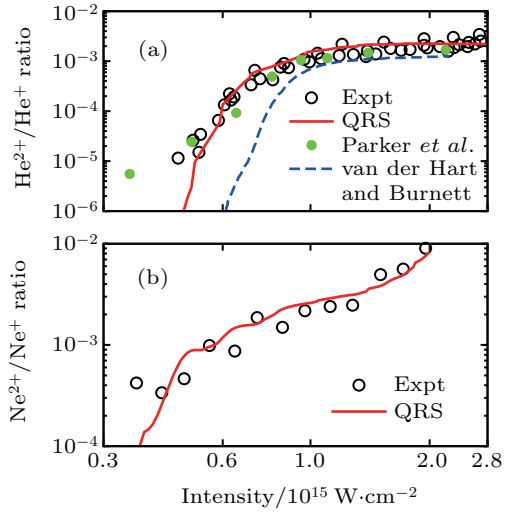


Fig. 7. Ratio between double and single ionization as a function of intensity for (a) He in a 120 fs pulse with a wavelength of 390 nm, and (b) Ne in a 40 fs pulse with a wavelength of 400 nm. In (a), the present simulations are compared with the experimental data of Sheehy *et al*,[82] the TDSE calculations of Parker *et al*,[12] and the calculations of van der Hart and Burnett[40] based on the rescattering model. All experimental data points were shifted to higher intensity by 50%, as suggested by Parker *et al*.[12] In (b), the present results are compared with the experimental data of Ekanayake *et al*.[83] Adapted from Ref. [36].

With the carefully prepared absolute double and single ionization yields, it is straightforward to obtain the double-to-single ionization ratio.

Using the improved QRS model, Chen *et al*.[35,36,38] have recently calculated the double-to-single ionization ratios for He and Ne in intense fields with various different laser parameters, and the numerical results were found to be in good accordance with the experimentally measured data.[5,82–85] Figure 7 shows the double-to-single ionization ratios simulated by the QRS model for He in a 120 fs pulse with a wavelength of 390 nm and for Ne in a 40 fs pulse with a wavelength of 400 nm, respectively. In both cases, the results of the QRS model are in remarkably good agreement with the experimental measurements[82,83] over the whole range of laser intensity. It should be noted that, in Fig. 7(a) the measured intensities are multiplied by 1.5, as suggested by Parker *et al*.[12] who performed the corresponding TDSE calculations, and in Fig. 7(b) the experimental data of the double-to-single ionization ratio for Ne were deduced from the total ionization yields of Ne^{2+} and Ne^+ measured by Ekanayake *et al*.[83] One can see from Fig. 7(a) that the QRS model also reproduces the TDSE results of Parker *et al*.[12] very well, except for the intensities below 5.0×10^{14} W/cm^2. However, the calculations of van

der Hart and Burnett,[40] which are also based on the rescattering model, predict a lower intensity dependence especially at low intensities.

Very recently, the QRS model has also been employed to investigate the pulse-duration dependence of the double-to-single ionization ratio of Ne by intense 780-nm and 800-nm laser fields.[38]

3.4. Correlated electron momentum distribution

While the early measurements of the total ionization yields for doubly charged ions greatly stimulated the investigation of NSDI, the experimental data could only give little insight into the ionization mechanism compared to the correlated two-electron momentum distributions (CMD). Since the first measurement performed by Weber *et al.*[77] at the turn of this century, the CMD have been shown to provide the most detailed information of NSDI, and hence yield direct and intuitive insight into the dynamics of laser–atom interaction.

In 2010, just two years after it was first development for HATI and HHG,[86] the QRS model was quickly extended to the simulations of CMD for NSDI of He, Ne, and Ar atoms.[31,32,87] Different from the calculations of total ionization yields for doubly charged ions in which only the TCSs for electron impact excitation and electron impact ionization of the parent ion are needed, in the simulations of CMD for NSDI, it is necessary to evaluate the DCSs for the corresponding inelastic collision processes. Consequently, the numerical procedures become much more complicated. Very recently, the QRS model was further improved and the NSDI processes of He were revisited.[37,39]

Within the framework of the present QRS model, the CMD for recollisional $(e,2e)$ process and recollisional excitation with subsequent tunneling of the second electron are simulated separately.

3.4.1. Recollisional $(e,2e)$ process

According to the QRS model, the CMD for laser-induced $(e,2e)$ collision in NSDI can be factorized as a product of the RWP and the field-free differential cross section for ionization of the parent ion by the impact of the laser-induced returning electron. In experiment, the CMD for NSDI are measured only for the momentum components along the laser polarization axis for the two outgoing electrons. Thus, to compare with experiment, the calculated TDCS for the laser-free $(e,2e)$ process needs to be projected on the polarization axis. For a given incident energy, the two-electron momentum spectra along the incident direction for the laser-free $(e,2e)$ process can be obtained by integrating the TDCS over ϕ_2 and E_2

$$Y_{E_i}^{e2e}(k_1^{||},k_2^{||}) = \frac{4\pi}{k_1 k_2}\int_0^{E_2^{\max}} \mathrm{d}E_2 \int_0^{\pi} \mathrm{d}\phi_2 \frac{\mathrm{d}^3\sigma_{e2e}}{\mathrm{d}\Omega_1 \mathrm{d}\Omega_2 \mathrm{d}E_2}\Big|_{\phi_1=0}, \quad (89)$$

where $E_2^{\max} = E_i - I_\mathrm{p}$, and I_p is the ionization potential of the parent ion. In Eq. (89), we set $\phi_1 = 0$ owing to the cylindrical symmetry of the TDCS, and the integration over ϕ_2 is performed only from 0 to π since the TDCS is symmetric about the plane formed by $\boldsymbol{k}_1$ and $\boldsymbol{k}_i$.

For laser-induced recollisional $(e,2e)$ process, the two electrons are still under the influence of the laser field after the collision, and thus at the end of the laser pulse each electron will gain an additional momentum $-A_r$, where A_r is the vector potential at the time when the recollision takes place. Therefore, by using the relation in Eq. (77) for each of the two outgoing electrons, the CMD for recollisional $(e,2e)$ process in a strong field at an intensity I can be expressed by

$$D_{E_i,I}^{e2e}(p_1^{||},p_2^{||}) = Y_{E_i}^{e2e}(k_1^{||}-A_r, k_2^{||}-A_r), \quad (90)$$

where $p_1^{||}$ and $p_2^{||}$ are the parallel momenta of the two correlated electrons along the laser polarization, respectively.

Based on the classical simulation[28] for HATI in which laser-induced elastic scattering takes place, the vector potential A_r at the collision time is approximately determined by the relation in Eq. (78). Nevertheless, for laser-induced inelastic collision of the returning electron with the parent ion, as discussed in Subsection 3.2, the threshold energy could be lowered due to the presence of electric field. Since it is extremely formidable to perform the actual numerical calculations including the lowering of the threshold energy, an alternative strategy was suggested by van der Hart and Burnett[40] in which it was assumed that the energy of the incoming electron with respect to the maximum of the barrier in the atomic and electric potential corresponds to the incoming electron energy in the field-free case. Based on this assumption, equation (78) should be modified and rewritten as

$$|A_r| = \sqrt{2(E_i - \Delta E)}/1.26, \quad (91)$$

where $\Delta E = |V_\mathrm{b}|$ and V_b is given by Eq. (84).

To obtain the CMD for a given intensity, one has to consider the contributions from all collisions at different incident energies weighted by the RWP. This gives

$$D_I^{e2e}(p_1^{||},p_2^{||}) = \int_{I_\mathrm{p}}^{\infty} \mathrm{d}E_i D_{E_i,I}^{e2e}(p_1^{||},p_2^{||}) W_I(E_i - \Delta E), \quad (92)$$

where $W_I(E_i - \Delta E)$ is the RWP in the laser field at a single intensity I, which can be calculated by using SFA2. We emphasize that the lowering of threshold has been taken into account in Eq. (92).

Finally, to compare with experimental measurements, the integration over the focus volume should be performed

$$\bar{D}_{I_0}^{e2e}(p_1^{||},p_2^{||}) = \int_0^{I_0} D_I^{e2e}(p_1^{||},p_2^{||}) \left(\frac{\partial V}{\partial I}\right) \mathrm{d}I, \quad (93)$$

where I_0 is the peak intensity of the laser field.

We comment that the above numerical procedures for recollisional $(e,2e)$ in NSDI are directly applicable to all rare gas

atoms except that for He the spin conservation should be considered such that in Eq. (89) the singlet TDCS should be used. Clearly, the simulated CMD highly depends on the theoretical models employed to calculate the TDCS for laser-free electron impact ionization of the parent ion. For example, very recently, Chen *et al.*[37] have presented numerical simulations on the CMD for recollisional $(e,2e)$ process in NSDI of helium by a 800 nm laser field at an intensity around 4.5×10^{14} W/cm^2 based on the improved QRS model. In the TDCS calculations for $(e,2e)$ on He^+, several theoretical models, which are referred to as 2C, 3C, 4C, DS3C, and DS4C, respectively (see Subsection 2.6 and Ref. [37] for details), have been used. The simulated results were compared with experimental measurements of Staudte *et al*,[14] as shown in Fig. 8. It has been found that while the postcollision Coulomb interaction is responsible for the observed fingerlike structure, the precollision Coulomb interaction changes the orientation of the two fingers from V-type to parallel, and the dynamic screening of the three-body Coulomb interactions in the final state reduces the separation of the two fingers.

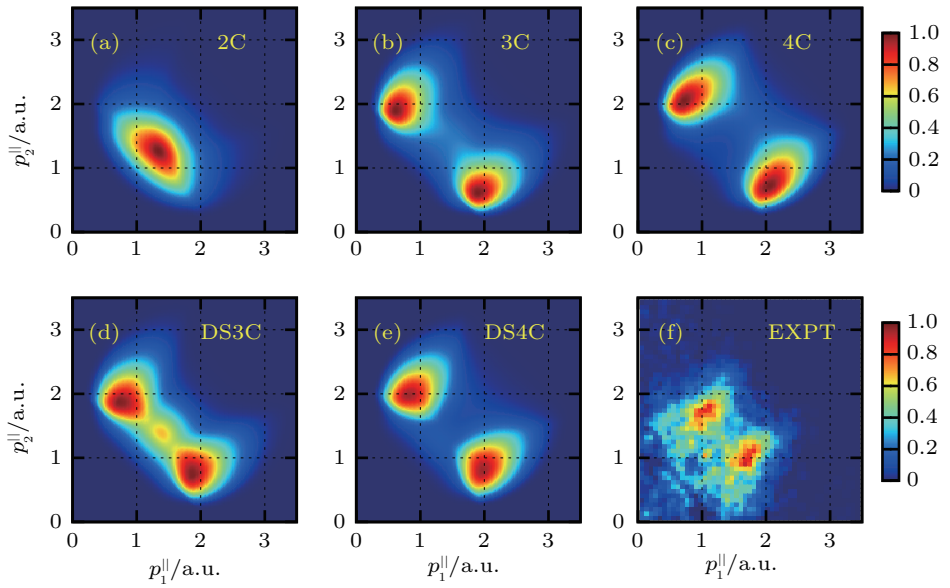


Fig. 8. Normalized correlated two-electron momentum distributions for laser-induced recollisional $(e,2e)$ process on He^+ in 45 fs and 800 nm laser pulses at the peak intensity 4.0×10^{14} W/cm^2. The momentum components along the polarization direction are shown. The potential change due to the presence of electric field at the recollision time is taken into account, and the focal volume integral is performed. The calculated results are obtained by using the theoretical models (a) 2C, (b) 3C, (c) 4C, (d) DS3C, and (e) DS4C, respectively. The experimental measurements shown in (f) were performed by Staudte *et al*.[14] Adapted from Ref. [37].

3.4.2. Recollisional excitation-tunneling process

Apart from recollisional $(e,2e)$, another main mechanism in NSDI is recollisional excitation-tunneling. At a single peak intensity, the CMD for recollisional excitation-tunneling of atoms in a linearly polarized laser pulse can be expressed as a product of the parallel momentum distribution for the scattered electron after recollisional excitation and the parallel momentum distribution for tunneling-ionized electron from the excited state.

The parallel momentum distribution for the scattered electron after excitation at a given incident energy E_i can be obtained by projecting the DCS $\mathrm{d}\sigma_{\rm exc}/\mathrm{d}\Omega$ for laser-free electron impact excitation of parent ion onto the polarization direction

$$Y_{E_i}^{\rm exc}(k_1^{||}) = \frac{2\pi}{k_1}\frac{\mathrm{d}\sigma_{\rm exc}}{\mathrm{d}\Omega}, \tag{94}$$

where k_1 is the momentum of the scattered electron and $k_1^{||} = k_1\cos\theta$ with θ being the scattering angle. Again, according to the QRS model, the corresponding parallel momentum distribution for the recollisional excitation process taking place in a strong laser field at an intensity I can be obtained from Eq. (94) by shifting the momentum of the projectile electron by $-A_r$

$$D_{E_i,I}^{\rm exc}(p_1^{||}) = Y_{E_i}^{\rm exc}(k_1^{||} - A_r), \tag{95}$$

where A_r is the vector potential at the instant of recollision, which is related to the returning (incident) electron energy by Eq. (91).

For tunneling ionization of electron from excited state of the parent ion, several theoretical models, such as ADK, PPT, SFA, and TDSE, can be used to evaluate the parallel momentum distribution. Among all of these theoretical methods, the ADK model is the simplest one. Using the ADK model, the ionization rate, with the depletion effect taken into account, can be expressed as

$$Y_I^{\rm tun}(t) = W\left[|F(t)|\right] \mathrm{e}^{-\int_{t_0}^{t} W\left[|F(t')|\right]\mathrm{d}t'}, \tag{96}$$

where $W\left[|F(t)|\right]$ is the modified ADK rate given by Eq. (2) in Ref. [46]. Assuming that the initial velocity of the tunneling

electron is zero, the momentum spectrum for single ionization of the parent ion is given by

$$D_I^{\rm tun}(p_2^{||}) = D_I^{\rm tun}[-A(t)] = \frac{1}{|E(t)|} Y_I^{\rm tun}(t). \quad (97)$$

With the parallel momentum distributions $D_{E_i,I}^{\rm excit}(p_1^{||})$ for excitation and $D_I^{\rm tun}(p_2^{||})$ for tunneling ionization, the CMD for laser-induced electron impact excitation at incident energy E_i with subsequent tunneling ionization in the laser field at a peak intensity I reads

$$D_{E_i,I}^{\text{exc-tun}}(p_1^{||}, p_2^{||}) = D_{E_i,I}^{\rm exc}(p_1^{||}) \times D_I^{\rm tun}(p_2^{||}). \quad (98)$$

For a given intensity, in principle, excitation takes place as long as the kinetic energy of the returning electron is larger than the lowered threshold energy. Therefore, similar to recollisional $(e,2e)$, an integral over E_i should be performed to account for the contributions from collisions at all incident energies

$$D_I^{\text{exc-tun}}(p_1^{||}, p_2^{||}) = \int_{I_{\rm exc}}^{\infty} {\rm d}E_i D_{E_i,I}^{\text{exc-tun}}(p_1^{||}, p_2^{||}) W_I(E_i - \Delta E), \quad (99)$$

where $I_{\rm exc}$ is the threshold energy for excitation.

Finally, to compare with experiment, an integration over the focus volume should be performed according to

$$\bar{D}_{I_0}^{\text{exc-tun}}(p_1^{||}, p_2^{||}) = \int_0^{I_0} D_I^{\text{exc-tun}}(p_1^{||}, p_2^{||}) \left(\frac{\partial V}{\partial I}\right) {\rm d}I, \quad (100)$$

where I_0 is the peak intensity of the laser field.

As indicated in Eqs. (98) and (99), the CMD for recollisional excitation-tunneling consists of the parallel momentum distribution for the returning electron after collision, the parallel momentum distribution for the electron ionized from the excited state of the parent ion, and the momentum (energy) distribution of the returning electron before collision. Each of the three ingredients plays an important role in the simulations of the CMD.

In a previous work, the CMD for recollisional excitation-tunneling in NSDI of He was simulated by Chen *et al.*[32] who used the DWBA model to calculate the DCSs for electron impact excitation of He^+ while the parallel momentum distribution for tunneling-ionization was evaluated by using the modified ADK model. However, it is well known that, the total cross sections predicted by the DWBA often exceed the experimental values significantly at low energies, even though the angular distribution of the DCS from DWBA calculations is typically in fairly good agreement with experiment. On the other hand, a damping factor was introduced empirically in the modified ADK model. Unfortunately, the damping factor is not available for ionization from the excited states although it has been well estimated for ionization from the ground state of a few atoms and ions.[46]

Very recently, the recollisional excitation-tunneling process in NSDI of helium in 800 nm laser pulse was revisited and the CMD measured by Staudte *et al.*[14] was re-simulated by Chen *et al.*[39] using the improved QRS model. In those

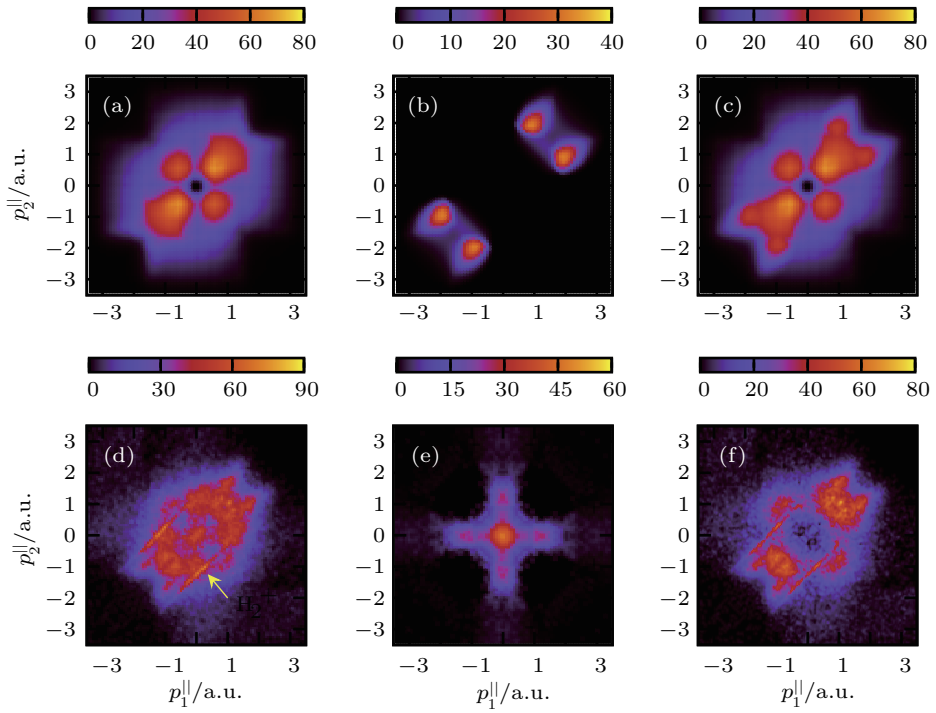


Fig. 9. Comparison of the simulated correlated parallel momentum spectra with the experimental measurements.[14] The first row shows the simulated results for NSDI of He in the laser field at the peak intensity of 3.5×10^{14} W/cm^2: (a) excitation-tunneling from all excited states of $n = 2$ and 3, (b) $(e,2e)$, (c) sum of excitation-tunneling and $(e,2e)$. The second row displays the experimental data: (d) full experimental measurements, (e) spectra excluding $(e,2e)$ and excitation-tunneling, (f) spectra deduced from (d) with (e) deducted. The calculations include the integration over the focal volume of the laser. Adapted from Ref. [39].

CMD simulations, the DCSs for electron impact excitation of He^+ were calculated using the state-of-the-art many-electron R-matrix theory, and the tunneling ionization rates for electrons in the excited states were evaluated by solving the TDSE. The calculated CMD is displayed in Fig. 9(a), which demonstrates that the fourfold symmetry with regard to the parallel momentum components is broken. This is in contradiction to the prevalent view that the correlation pattern for excitation-tunneling in NSDI is symmetric with respect to the coordinate axes. Nevertheless, in order to compare with the entire CMD measured in the experiment, the momentum distribution for the recollisional $(e,2e)$ process has to be included. Figure 9(b) shows the CMD for the recollisional $(e,2e)$ process in NSDI of He.[37] By summing the CMD in Figs. 9(a) and 9(b), the predicted CMD for NSDI of He including both recollisional $(e,2e)$ and excitation-tunneling is obtained, as depicted in Fig. 9(c). Figure 9(d) shows the original experimental data of the CMD for NSDI of He.[14] However, by comparing the simulated CMD in Fig. 9(c) with the experimental data shown in Fig. 9(d), one observes that the populations along the axes in the experimental CMD are not reproduced by the QRS model. This is due to the fact that the kinematically allowed regime for the correlated electron momentum components parallel to the laser polarization axis in excitation-tunneling does not reach this region for the case considered here, even with the potential change taken into account. It has been argued[32] that an additional mechanism might be responsible for the distribution along the axes in the CMD which can be separated from the entire CMD measured in the experiment, as displayed in Fig. 9(e). By deducting the CMD in Fig. 9(e) from that in Fig. 9(d), one obtains the "refined" experimental CMD owing to the mechanisms of recollisional ionization and excitation-tunneling only, as shown in Fig. 9(f). Therefore, the simulated CMD in Fig. 9(c) should be compared directly with the corresponding CMD of experiment in Fig. 9(f), and the comparison demonstrates that the theoretical predictions are in fairly good agreement with the experiment.

4. Conclusion and perspectives

We have reviewed the quantitative rescattering (QRS) model for nonsequential double ionization (NSDI) of atoms in strong laser field. With the recent improvement, i.e., by taking into account the lowering of threshold energy due to the presence of electric field, the QRS model has been employed to simulate the total yield of the doubly charged ion as a function of laser intensity, and the correlated two-electron momentum distributions (CMD) for recollisional $(e,2e)$ and excitation-tunneling as well. Since the obtained results highly depend on the scattering cross sections involved in the simulations, the QRS model provides a stringent test of the quantum collision theories for the traditional laser-free scattering processes. It has been found that with the carefully prepared accurate total and differential cross sections for both electron impact ionization and electron impact excitation, the total yields of doubly charged ion and the CMD for recollisional $(e,2e)$ and excitation-tunneling measured in experiments can be well predicted by the QRS model. However, to simulate the double-to-single ionization ratio, both the returning electron wave packet calculated by using the SFA2 and the total yield for single ionization evaluated by using the simple models, such as ADK, PPT and SFA, need to be calibrated according to the corresponding results by solving the TDSE for short laser pulses. This calibration reflects the consistency of the QRS model for different types of recollision processes.

Despite the great success of the QRS model in making quantitative predictions on recollision phenomena including NSDI, there is still a lot of space left for improvement. For example, within the framework of the QRS model, it is still hard to predict the momentum distributions for capture-tunneling, although the mechanism can be interpreted qualitatively.[32] Furthermore, the deficiency of the QRS model remains that the quantum interference effects in NSDI at low intensities[88–91] are absent in the model results. This is mainly due to the fact that the transition amplitudes are not available when the ADK model is used to evaluate the parallel momentum distributions of the tunneling electron. In a very recent work,[39] the parallel momentum distributions of the tunneling electron are obtained by projecting the two-dimensional momentum spectra, evaluated by solving the TDSE, onto the polarization direction. Since the TDSE not only provides the probabilities but also the necessary amplitudes, a way to study the interference effect in NSDI based on the QRS model has been paved.

So far, the QRS model has only been used for treating NSDI in linearly polarized laser field. In the recent years, many efforts have shifted to NSDI in elliptically polarized laser field,[92] two-color laser field,[93] and especially counter-rotating circularly polarized two-color field[94–96] for which the semiclassical model has been widely employed. With the established validity of the QRS model for HATI in two-color strong laser fields,[97,98] it is reasonable to expect that the QRS model could also be applied to NSDI in two-color fields. This is, of course, a part of our work in the near future.

References

[1] L'Huillier A, Lompre L A, Mainfray G and Manus C 1982 *Phys. Rev. Lett.* **48** 1814

[2] L'Huillier A, Lompre L A, Mainfray G and Manus C 1983 *Phys. Rev. A* **27** 2503

[3] Fittinghoff D N, Bolton P R, Chang B and Kulander K C 1992 *Phys. Rev. Lett.* **69** 2642

[4] Walker B, Mevel E, Yang B, Breger P, Chambaret J P, Antonetti A, DiMauro L F and Agostini P 1993 *Phys. Rev. A* **48** R894

[5] Walker B, Sheehy B, DiMauro L F, Agostini P, Schafer K J and Kulander K C 1994 *Phys. Rev. Lett.* **73** 1227

[6] Corkum P B 1993 *Phys. Rev. Lett.* **71** 1994

[7] Weber Th, Weckenbrock M, Staudte A, Spielberger L, Jagutzki O, Mergel V, Afaneh F, Urbasch G, Vollmer M, Giessen H and Dörner R 2000 *Phys. Rev. Lett.* **84** 443

[8] Weber Th, Giessen H, Weckenbrock M, Urbasch G, Staudte A, Spielberger L, Jagutzki O, Mergel V, Vollmer M and Dörner R 2000 *Nature* **405** 658

[9] Feuerstein B, Moshammer R, Fischer D, Dorn A, Schröter C D, Deipenwisch J, Crespo Lopez-Urrutia J R, Höhr C, Neumayer P, Ullrich J, Rottke H, Trump C, Wittmann M, Korn G and Sandner W 2001 *Phys. Rev. Lett.* **87** 043003

[10] Becker W, Liu X, Ho P J and Eberly J H 2012 *Rev. Mod. Phys.* **84** 1011

[11] Peng L Y, Jiang W C, Geng J W, Xiong W H and Gong Q H 2015 *Phys. Rep.* **575** 1

[12] Parker J S, Moore L R, Dundas D and Taylor K T 2000 *J. Phys. B* **33** L691

[13] Parker J S, Doherty B J S, Taylor K T, Schultz K D, Blaga C I and DiMauro L F 2006 *Phys. Rev. Lett.* **96** 133001

[14] Staudte A, Ruiz C, Schöffler M, Schössler S, Zeidler D, Weber Th, Meckel M, Villeneuve D M, Corkum P B, Becker A and Dörner R 2007 *Phys. Rev. Lett.* **99** 263002

[15] Efimov D K, Maksymov A, Prauzner-Bechcicki J S, Thiede J H, Eckhardt B, Chacón A, Lewenstein M and Zakrzewski J 2018 *Phys. Rev. A* **98** 013405

[16] Haan S L, Breen L, Karim A and Eberly J H 2006 *Phys. Rev. Lett.* **97** 103008

[17] Zhou Y, Liao Q and Lu P 2010 *Phys. Rev. A* **82** 053402

[18] Zhang Z, Bai L and Zhang J 2014 *Phys. Rev. A* **90** 023410

[19] Lewenstein M, Kulander K C, Schafer K J and Bucksbaum P H 1995 *Phys. Rev. A* **51** 1495

[20] Chen Z, Morishita T, Le A T and Lin C D 2007 *Phys. Rev. A* **76** 043402

[21] Becker A and Faisal F H M 2005 *J. Phys. B* **38** R1

[22] Schafer K J, Yang B, DiMauro L F and Kulander K C 1993 *Phys. Rev. Lett.* **70** 1599

[23] Chen J, Liu J, Fu L B and Zheng W M 2000 *Phys. Rev. A* **63** 011404

[24] Fu L B, Liu J, Chen J and Chen S G 2001 *Phys. Rev. A* **63** 043416

[25] Wu M Y, Wang Y L, Liu X J, Li W D, Hao X L and Chen J 2013 *Phys. Rev. A* **87** 013431

[26] Wang Y L, Xu S P, Quan W, Gong C, Lai X Y, Hu S L, Liu M Q, Chen J and Liu X J 2016 *Phys. Rev. A* **94** 053412

[27] Chen Z, Li X, Sun X, Hao X and Chen J 2017 *J. Phys. B* **50** 245601

[28] Chen Z, Le A T, Morishita T and Lin C D 2009 *Phys. Rev. A* **79** 033409

[29] Chen Z, Le A T, Morishita T and Lin C D 2009 *J. Phys. B* **42** 061001

[30] Micheau S, Chen Z, Le A T and Lin C D 2009 *Phys. Rev. A* **79** 013417

[31] Chen Z, Liang Y and Lin C D 2010 *Phys. Rev. Lett.* **104** 253201

[32] Chen Z, Liang Y and Lin C D 2010 *Phys. Rev. A* **82** 063417

[33] Lin C D, Le A T, Jin C and Wei H 2018 *Attosecond and Strong-Field Physics Principles and Applications* (Cambrige: Cambrige University Press)

[34] Lin C D, Le A T, Jin C and Wei H 2018 *J. Phys. B* **51** 104001

[35] Chen Z, Zheng Y, Yang W, Song X, Xu J, DiMauro L F, Zatsarinny O, Bartschat K, Morishita T, Zhao S F and Lin C D 2015 *Phys. Rev. A* **92** 063427

[36] Chen Z, Li X, Zatsarinny O, Bartschat K and Lin C D 2018 *Phys. Rev. A* **97** 013425

[37] Chen Z, Wang Y, Zhang L and Jia X 2019 *Phys. Rev. A* **99** 033401

[38] Chen Z, Zhang L, Wang Y, Zatsarinny O, Bartschat K, Morishita T and Lin C D 2019 *Phys. Rev. A* **99** 043408

[39] Chen Z, Wang Y, Morishita T, Hao X, Chen J, Zatsarinny O and Bartschat K 2019 *Phys. Rev. A* **100** 023405

[40] van der Hart H W and Burnett K 2000 *Phys. Rev. A* **62** 013407

[41] Grasbon F, Paulus G G, Walther H, Villoresi P, Sansone G, Stagira S, Nisoli M and Silvestri S De 2003 *Phys. Rev. Lett.* **91** 173003

[42] Krausz F and Ivanov M 2009 *Rev. Mod. Phys.* **81** 163

[43] Keldysh L V 1964 *Zh. Eksp. Teor. Fiz.* **47** 1945; 1965 *Sov. Phys. JETP* **20** 1307

[44] Ammosov M V, Delone N B and Krainov V P 1986 *Zh. Éksp. Teor. Fiz.* **91** 2008; 1986 *Sov. Phys. JETP* **64** 1191

[45] Tong X M, Zhao Z X and Lin C D 2002 *Phys. Rev. A* **66** 033402

[46] Tong X M and Lin C D 2005 *J. Phys. B* **38** 2593

[47] Perelomov A M, Popov V S and Terent'ev M V 1967 *Sov. Phys. JETP* **24** 207

[48] Fu Y Z, Zhao S F and Zhou X X 2012 *Chin. Phys. B* **21** 113101

[49] Lai Y H, Xu J, Szafruga U B, Talbert B K, Gong X, Zhang K, Fuest H, Kling M F, Blaga C I, Agostini P and DiMauro L F 2017 *Phys. Rev. A* **96** 063417

[50] Becker W, Grasbon F, Kopold R, Milošević D B, Paulus G G and Walther H 2002 *Adv. At. Mol. Opt. Phys.* **48** 35

[51] Guo J Z, Chen Z J and Zhou X X 2014 *Chin. Phys. B* **23** 043201

[52] Milošević D B and Ehlotzky F 1998 *Phys. Rev. A* **57** 5002

[53] C. Figueira de Morisson Faria, Schomerus H and Becker W 2002 *Phys. Rev. A* **66** 043413

[54] Tong X M and Chu S I 1997 *Chem. Phys.* **217** 119

[55] Morishita T, Chen Z, Watanabe S and Lin C D 2007 *Phys. Rev. A* **75** 023407

[56] Harris D O, Engerholm G G and Gwinn W D 1965 *J. Chem. Phys.* **43** 1515

[57] Dickinson A S and Certain P R 1968 *J. Chem. Phys.* **49** 4209

[58] Light J C and Walker R B 1976 *J. Chem. Phys.* **65** 4272

[59] Liang Y 2010 *Phys. Rev. A* **82** 055403

[60] Chen Z J, Ye J M and Xu Y B 2015 *Chin. Phys. B* **24** 103203

[61] Schiff L I 1968 *Quantum Mechanics* (3rd Edn.) (New York: McGraw-Hill) p. 145,

[62] Joachain C J 1983 *Quantum Collision Theory* (3rd Edn.) (Amsterdam: North-Holland) p. 144

[63] Lai Z J, Chen D F, Pan L Q, Jiang X H, Xu Y L and Chen Z J 2014 *J. At. Mol. Sci.* **5** 311

[64] Zeman V and Bartschat K 1997 *J. Phys. B* **30** 4609

[65] Bray I and Stelbovics A T 1992 *Phys. Rev. A* **46** 6995

[66] Liang Y, Chen Z, Madison D H and Lin C D 2011 *J. Phys. B* **44** 085201

[67] Chen Z, Madison D H, Whelan C T and Walters H R J 2004 *J. Phys. B* **37** 981

[68] Prideaux A and Madison D H 2003 *Phys. Rev. A* **67** 052710

[69] Prideaux A, Madison D H and Bartschat K 2005 *Phys. Rev. A* **72** 032702

[70] Brauner M, Briggs J S and Klar H 1989 *J. Phys. B* **22** 2265

[71] Jia X, Shi Q, Chen Z, Chen J and Xu K 1997 *Phys. Rev. A* **55** 1971

[72] Berakdar J and Briggs J S 1994 *Phys. Rev. Lett.* **72** 3799

[73] Chen Z, Shi Q, Zhang S, Chen J and Xu K 1997 *Phys. Rev. A* **56** R2514

[74] Augst S, Meyerhofer D D, Strickland D and Chin S L 1991 *J. Opt. Soc. Am. B* **8** 858

[75] Colosimo P, Doumy G, Blaga C I, Wheeler J, Hauri C, Catoire F, Tate J, Chirla R, March A M, Paulus G G, Muller H G, Agostini P and Dimauro L F 2008 *Nat. Phys.* **4** 386

[76] Corkum P B and Krausz F 2007 *Nat. Phys.* **3** 381

[77] Weber T, Giessen H, Weckenbrock M, Urbasch G, Staudte A, Spielberger L, Jagutzki O, Mergel V, Vollmer M and Dörner R 2000 *Nature* **405** 658

[78] Xu J, Zhou H L, Chen Z and Lin C D 2009 *Phys. Rev. A* **79** 052508

[79] Blaga C I, Xu J, DiChiara A D, Sistrunk E, Zhang K, Agostini P, Miller T A, DiMauro L F and Lin C D 2012 *Nature* **483** 194

[80] Xu J, Blaga C I, DiChiara A D, Sistrunk E, Zhang K, Chen Z, Le A-T, Morishita T, Lin C D, Agostini P and DiMauro L F 2012 *Phys. Rev. Lett.* **109** 233002

[81] Zatsarinny O and Bartschat K 2013 *J. Phys. B* **46** 112001

[82] Sheehy B, Lafon R, Widmer M, Walker B, DiMauro L F, Agostini P A and Kulander K C 1998 *Phys. Rev. A* **58** 3942

[83] Ekanayake N, Luo S, Wen B L, Howard L E, Wells S J, Videtto M, Mancuso C, Stanev T, Condon Z, LeMar S, Camilo A D, Toth R, Crosby WB, Grugan P D, Decamp M F and Walker B C 2012 *Phys. Rev. A* **86** 043402

[84] Larochelle S, Talebpoury A and Chin S L 1998 *J. Phys. B* **31** 1201

[85] Bhardwaj V R, Aseyev S A, Mehendale M, Yudin G L, Villeneuve D M, Rayner D M, Ivanov M Y and Corkum P B 2001 *Phys. Rev. Lett.* **86** 3522

[86] Morishita T, Le A T, Chen Z and Lin C D 2008 *Phys. Rev. Lett.* **100** 013903

[87] Chen Z, Liang Y, Maidosn D H and Lin C D 2011 *Phys. Rev. A* **84** 023414

[88] Hao X L, Chen J, Li W D, Wang B, Wang X and Becker W 2014 *Phys. Rev. Lett.* **112** 073002

[89] Maxwell A S and Figueira de Morisson Faria C 2015 *Phys. Rev. A* **92** 023421

[90] Maxwell A S and Figueira de Morisson Faria C 2016 *Phys. Rev. Lett.* **116** 143001

[91] Quan W, Hao X L, Wang Y L, Chen Y J, Yu S G, Xu S P, Xiao Z L, Sun R P, Lai X Y, Hu S L, Liu M Q, Shu Z, Wang X D, Li W D, Becker W, Liu X J and Chen J 2017 *Phys. Rev. A* **96** 032511

[92] Kang H, Henrichs K, Kunitski M, Wang Y, Hao X, Fehre K, Czasch A, Eckart S, Schmidt L P H, Schöffler M, Jahnke T, Liu X and Döner R 2018 *Phys. Rev. Lett.* **120** 223204

[93] Mancuso C A, Dorney K M, Hickstein D D, Chaloupka J L, Ellis J L, Dollar F J, Knut R, Grychtol P, Zusin D, Gentry C, Gopalakrishnan M, Kapteyn H C and Murnane M M 2016 *Phys. Rev. Lett.* **117** 133201

[94] Chaloupka J L and Hickstein D D 2016 *Phys. Rev. Lett.* **116** 143005

[95] Huang C, Zhong M and Wu Z 2018 *Opt. Express* **26** 26045

[96] Ma X, Zhou Y, Chen Y, Li M, Li Y, Zhang Q and Lu P 2019 *Opt. Express* **27** 1825

[97] Ray D, Chen Z, De S, Cao W, Litvinyuk I V, Le A T, Lin C D, Kling M F and Cocke C L 2011 *Phys. Rev. A* **83** 013410

[98] Chen Z 2011 *J. Phys. B* **44** 245601